Università degli Studi di Messina

DIPARTIMENTO DI SCIENZE MATEMATICHE E INFORMATICHE, SCIENZE FISICHE E SCIENZE DELLA TERRA

DOTTORATO DI RICERCA IN FISICA *XXIX* CICLO

The Calibration System of the E989 Experiment at Fermilab
PhD Thesis
Antonio ANASTASI

SSD:FIS04

PhD COORDINATOR:
Prof. **Lorenzo TORRISI**

TUTOR:
Dr. **Giuseppe MANDAGLIO**
CO-TUTOR:
Dr. **Graziano VENANZONI**
CO-TUTOR:
Prof. **David HERTZOG**

TRIENNIO 2014/2016

Contents

Introduction

The muon anomaly a_μ is one of the most precise quantity known in physics experimentally and theoretically. The high level of accuracy permits to use the measurement of a_μ as a test of the Standard Model comparing with the theoretical calculation. After the impressive result obtained at Brookhaven National Laboratory in 2001 with a total accuracy of 0.54 ppm, a new experiment E989 is under construction at Fermilab, motivated by the difference of $a_\mu^{exp} - a_\mu^{SM} \sim 3\sigma$. The purpose of the E989 experiment is a fourfold reduction of the error, with a goal of 0.14 ppm, improving both the systematic and statistical uncertainty. With the use of the Fermilab beam complex a statistic of $\times$ 21 with respect to BNL will be reached in almost 2 years of data taking improving the statistical uncertainty to 0.1 ppm. Improvement on the systematic error involves the measurement technique of ω_a and ω_p, the anomalous precession frequency of the muon and the Larmor precession frequency of the proton respectively. The measurement of ω_p involves the magnetic field measurement and improvements on this sector related to the uniformity of the field should reduce the systematic uncertainty with respect to BNL from 170 ppb to 70 ppb. A reduction from 180 ppb to 70 ppb is also required for the measurement of ω_a; new DAQ, a faster electronics and new detectors and calibration system will be implemented with respect to E821 to reach this goal. In particular the laser calibration system will reduce the systematic error due to

gain fluctuations of the photodetectors from 0.12 to 0.02 ppm. The 0.02 ppm limit on systematic requires a system with a stability of 10^{-4} on short time scale (700 μs) while on longer time scale the stability is at the percent level. The 10^{-4} stability level required is almost an order of magnitude better than the existing laser calibration system in particle physics, making the calibration system a very challenging item. In addition to the high level of stability a particular environment, due to the presence of a 14 m diameter storage ring, a highly uniform magnetic field and the detector distribution around the storage ring, set specific guidelines and constraints. This thesis will focus on the final design of the Laser Calibration System developed for the E989 experiment. Chapter 1 introduces the subject of the anomalous magnetic moment of the muon; chapter 2 presents previous measurement of g-2, while chapter 3 discusses the Standard Model prediction and possible new physics scenario. Chapter 4 describes the E989 experiment. In this chapter will be described the experimental technique and also will be presented the experimental apparatus focusing on the improvements necessary to reduce the statistical and systematic errors. The main item of the thesis is discussed in the last two chapters: chapter 5 is focused on the Laser Calibration system while chapter 6 describes the Test Beam performed at the Beam Test Facility of Laboratori Nazionali di Frascati from the 29th February to the 7th March as a final test for the full calibrations system. An introduction explain the physics motivation of the system and the different devices implemented. In the final chapter the setup used will be described and some of the results obtained will be presented.

Chapter 1

History of the magnetic moment

1.1 Magnetic Moment

Considering a distribution of electrical charges the scalar potential is given by a multipole expansion of the form:

$$V = \sum_{n=0}^{\infty} \frac{1}{r^{n+1}} \int (r')^n P_n(\cos\theta') \rho(\mathbf{r}') d^3\mathbf{r}', \tag{1.1}$$

where V indicates the potential observed at any point integrating over the charge distribution $\rho(\mathbf{r}')$ in the coordinate system of Fig. 1.1.

The lowest-order term corresponds to the field generated by a single point charge and it is referred to as monopole term; the second order term can be physically approximated to the dipole term, thus to the field produced by two oppositely charged point-like particles separated by a distance d[1]. In the same way the vector potential of a magnetic field can be expressed as a multipole

---

[1]Technically to have a pure dipole field the charge separation would have to go to zero, but considering distances much greater than d from the charge distribution is a good approximation.
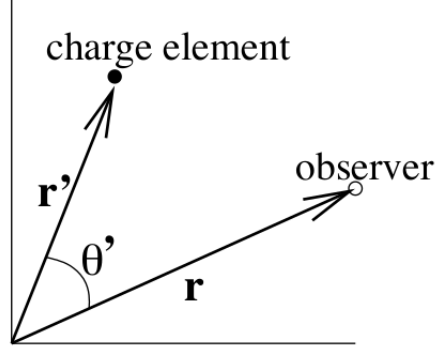
Figure 1.1: Coordinate system used in calculating potentials.

Figure 1.1: Coordinate system used in calculating potentials.

expansion[2]:

$$\mathbf{A} = \sum_{n=0}^{\infty} \frac{1}{r^{n+1}} \int (r')^n P_n(\cos\theta') \mathbf{J}(\mathbf{r}') d^3\mathbf{r}', \tag{1.2}$$

where the only difference is the replacement of the charge distribution $\rho(\mathbf{r}')$ of Eq. 1.1 with the current distribution $\mathbf{J}(\mathbf{r}')$, because magnetic fields are generated by moving charges. In this case the first term of the expansion is actually zero because of the non existence of the magnetic monopole; the first non-vanishing term is the second order term. It is important to clarify that this case is not exactly a dipole consisting of two point charges but rather a current loop as in Fig. 1.2.

The integral over space in Eq. 1.2 can be written as a simple line integral over all the infinitesimal elements $I d\boldsymbol{\ell}$; the first elements can be written as:

$$\mathbf{A} = I \left[\frac{1}{r} \oint d\boldsymbol{\ell} + \frac{1}{r^2} \oint r' \cos\theta' d\boldsymbol{\ell} + ... \right]. \tag{1.3}$$

As it should be the first term is actually 0 by definition. The second order term can be written differently just with some substitution:

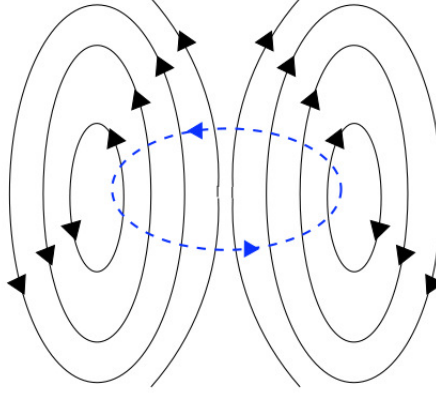[2]Using natural units: $\frac{h}{2\pi} = c = 1$.

Figure 1.2: Dipole magnetic field generated by a current loop.

Figure 1.2: Current loop generating a dipole magnetic field.

$$\mathbf{A}_{dip} = I \left[-\frac{1}{2}\hat{\mathbf{r}} + \oint (\mathbf{r} \times d\boldsymbol{\ell}) \right] = \frac{\boldsymbol{\mu} \times \hat{\mathbf{r}}}{r^2} \qquad (1.4)$$

where we can define the value of the *magnetic dipole moment* $\boldsymbol{\mu} = \frac{I}{2}\oint(\mathbf{r}\times d\boldsymbol{\ell})$ which can be simplified to $\mu = IA$ in the case of a current loop confined in a plane, where A is the total area enclosed by the current loop. This quantity represents the strength and the direction of the torque experienced by a current distribution placed in an external magnetic field $\boldsymbol{\tau}=\boldsymbol{\mu}\times\mathbf{B}$ with a potential energy U =- $\boldsymbol{\mu}\cdot\mathbf{B}$. This is a specific example used to introduce the quantity μ; the most general expression of the magnetic moment is given by:

$$\boldsymbol{\mu} = \frac{1}{2} \int (\mathbf{r}' \times \mathbf{J}(\mathbf{r}'))d^3\mathbf{r}'. \qquad (1.5)$$

Now considering the current as a series of i point-like particles each with a velocity $\mathbf{v}_i$ and charge q_i, it could be written as a sum $\mathbf{J} = \sum_i q_i\mathbf{v}_i\delta(\mathbf{r}' - \mathbf{r}_i)$; substituting this into Eq. 1.5 yields

$$\boldsymbol{\mu} = \frac{1}{2} \sum_i q_i(\mathbf{r}_i \times \mathbf{v}_i). \qquad (1.6)$$

Rewriting velocities in term of the momentum of the individual particles and considering the particles to be identical, the magnetic moment can be written as

$$\boldsymbol{\mu} = \frac{q}{2m}\mathbf{L}. \tag{1.7}$$

Eq. 1.7 shows the direct proportionality between the magnetic moment μ and the angular momentum $\mathbf{L}$.

1.2 Moving from classical to quantum era

The dawn of the 20th century was a period of strong innovation in the physics world. Names like Einstein, Schrödinger, Dirac, Pauli and Feynman, introduce a revolution in the way of understanding nature. In a few words the era of the atom and particle physics started. In 1922 the famous experiment by Stern and Gerlach showed that a beam of identical silver atoms passing through a magnetic field [1] emerged from it physically separated into two different bands along the axis of the magnetic field. What should be inferred by this result is that silver atoms have two possible magnetic moments, equal in magnitude but pointing to opposite directions. One possible source to this magnetic moments could be the electric charge of the nucleus that implies a scaling factor of $1/m_N$, where m_N is the mass of the nucleus. This scaling is not observed in silver and hydrogen experiments. This moved the interest to the orbiting electron in the atom as the possible culprit.

From spectroscopy experiment what came out was that a fourth quantum number, in addition to n, m and l introduced by quantum mechanics, was necessary to remove all the degeneracies in the experimental data. There was a big effort to explain data using different models (e.g Sommerfeld and Lande's

Ersatzmodel), which were only able to describe just some specific situation. The first solution to this problem, even if only qualitatively, was given by two young physicists, Samuel Goudsmith and George Uhlenbeck, where the idea of the *spin* with its value of $\pm\frac{1}{2}$ came out. Quantitatively the classical equation of the magnetic moment Eq. 1.7 underestimates the result of experiments like the Stern-Gerlach of a factor 2. The common practice to solve this problem was to incorporate this factor via the Lande *g-factor* or *gyromagnetic ratio*

$$\mu = g\frac{q}{2m_ec}\mathbf{S} \tag{1.8}$$

where $g=1$ for a classical system and $g=2$ referring to the electron. The rigorous mathematical description of spin came out thanks to Dirac in 1928 and his effort to create the relativistic variant of Schrödinger equation. Existence of spin was predicted together with the existence of anti-particles. The equation also predicts exactly the correct value of the magnetic moment for the electron with g=2 even when is not in the relativistic limit

$$\left(\frac{1}{2m_e}(\mathbf{P} - q\mathbf{A})^2 + \frac{q}{2m_e}\sigma \cdot \mathbf{B} - qA^0\right)\Psi_A = (E - m_e)\Psi_A. \tag{1.9}$$

Indeed recognizing the correspondence between the term proportional to $\mathbf{B}$ in Eq. 1.9 and the classical potential energy

$$U = -\boldsymbol{\mu} \cdot \mathbf{B} = \frac{q}{2m}\boldsymbol{\sigma} \cdot \mathbf{B}, \tag{1.10}$$

and solving for the magnetic moment the result is:

$$\boldsymbol{\mu} = -\frac{q}{2m_e}\boldsymbol{\sigma} = -2\frac{q}{2m_e}\mathbf{S} = -g\frac{q}{2m_e}\mathbf{S}. \tag{1.11}$$

To conclude this short description of the magnetic moment in the quantum era it is useful to mention that despite the advance of the quantum theories

even during the 30's there was still a lot to be learned about atoms and particles. 1932 was a great year of discovery because a wealth of new particles was discovered almost at the same time: Chadwick discovered the neutron [2], Anderson discovered the positron [3] as an example. After the discovery of the proton and neutron it was known that both were spin -$\frac{1}{2}$ particles and even if their magnetic moment was not yet measured it was natural to claim, giving the success of quantum mechanics, a value of g=2. Nevertheless it was discovered that the g-value of the proton was g=5.6 thanks to an experiment of Estermann and Stern [4] while Rabi measured the g-value for the neutron to be g=-3.8. Even if this seems a failure of the model at that time it was still not known that proton and neutron are not elementary particle; in fact their internal structure, composed by fractionally charged quarks, induces the magnetic moments to deviate strongly from the value 2 of a point-like particle.

1.3 The vacuum sea

Nowadays quantum field theory states that the vacuum is filled with a continuous flux of virtual particles which influence ordinary matter. If it were not for this sea of virtual particles, the g-value of the electron should be exactly 2 and any deviation will be a strong indication of an internal structure as in the case of proton and neutron. The interaction between ordinary matter and virtual particles leads to a slightly change in the observed magnetic moment of what would be for a simple bare particle without this kind of interaction. The fractional value to which g differs from 2 is called anomaly[3] and is defined as

---

[3]More specific can be defined as electron (a_e) or muon (a_μ) anomaly depending on which particle one refers to.
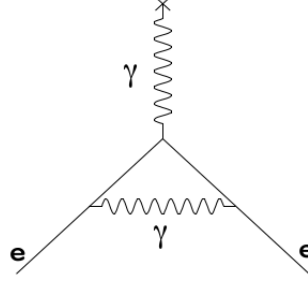
Figure 1.3: Feynman diagram for the lowest order self-interaction term.

$$a = \frac{g-2}{2}. \tag{1.12}$$

The first evidence of this anomaly is due to Kusch and Foley [5] who measured in 1948 a value of $g/2 = 1.00118(3)$, giving no space to doubt in the result given such a small error. Almost at the same time from the theory point of view Schwinger was able to calculate the first order correction to the magnetic moment g = 1.0016, which is within the quoted error of the Kusch and Foley experiment. Fig. 1.3 shows by the formalism of the Feynman diagram the lowest order self-interaction for the Schwinger term.

The calculation is a sum over terms of the fine structure constant $\alpha = 2\pi q^2/hc$. The best measurement of α comes from the comparison of the experimental value of the electron anomaly a_e^{exp} [6, 7, 8] and the theoretical evaluation of a_e^{SM}, where $\alpha^{-1} = 137.035999173(34)[0.25$ ppb] [9]. Certainly the uncertainty in the theory evaluation for the electron is dominated by the precision of this measurement. The most recent calculation comes from the computation of the fourth order in α [10, 11]

$$a_e^{theor} = \frac{\alpha}{2\pi} - 0.328478444000 \left(\frac{\alpha}{\pi}\right)^2 + 1.181234017 \left(\frac{\alpha}{\pi}\right)^3 + \quad (1.13)$$
$$-1.7502(384) \left(\frac{\alpha}{\pi}\right)^4 + 1.70(3) \times 10^{-12} = 0.0011596521465(240).$$

The experimental measurement on α_e has reached an incredible precision of 4 ppb even compared to the amazing precision obtained in the theoretical calculation of 20 ppb. The experimental setup used at Washington, by H. Dehmelt and his group [12], consist of a Penning trap and they were able to obtain the values of

$$a_{e^+}^{exp} = 0.0011596521884(43). \quad (1.14)$$

$$a_{e^-}^{exp} = 0.0011596521879(43) \quad (1.15)$$

with a difference between the theoretical and the experimental value of the electron anomaly at the 1.7 σ level.

Chapter 2

The muon g-2 experiments

In the middle of 20th century there was a growing interest on the muon. The results obtained for the neutron and proton g-2 can elicit that also a muon could have an internal structure because of its larger mass with respect to the electron. Muons have a lifetime $\tau_\mu = 2.2$ μs which makes it difficult to store them and analyze their spin. From the discovery of parity violation in 1957 [13, 14], it was understood that muons produced from pion decay are naturally polarized, providing a natural source of polarization for the experiment with muons. As another consequence of parity violation, the decaying of high energy electrons from a polarized muon source is preferentially in the same direction of the muon spin, providing a way to determine the spin direction of the muons as a function of time by counting experiment. Counting the number of decay electrons and applying an energy threshold, the fixed detector will measure a distribution in time of the following form

$$N(t) = N_0 e^{-\frac{t}{\tau_\mu}} [1 + A \cos(\omega_a t + \phi)], \qquad (2.1)$$

where N_0 is total population at time t=0, τ_μ is the muon lifetime, the value of A represents the asymmetry in the direction of the decaying particle[1], ω_a represents the anomalous precession frequency and the phase ϕ depends on the initial polarization of the muon beam. Moreover, sensitivity to exchange with heavy particles scales with the square of the leptons mass, giving to the muon an amplification factor of $(\frac{m_\mu}{m_e})^2 = 40000$ relative to the electron, thus increasing the sensitivity to new physics.

2.1 Early muon experiments

The first muon experiment was performed in 1957 by Garwin and collaborators at the Nevis cyclotron of the Columbia University [15]. Muons formed in flight from pion decays were stopped in a carbon target after passing one at time through an entrance counter. An external magnetic field applied to the target region causes the spin of the muon to precess. The precession could be increased or decreased tuning the magnitude of the external field. This experiment was able to determine a value for $g = 2.00 \pm 0.10$ for the muon, plotting the counts measured from the fixed counter as a function of the magnetic field following Eq. 2.2:

$$\omega_s = g\frac{eB}{2mc},\tag{2.2}$$

as shown in Fig. 2.1 (a). The precision obtained with this experiment was not sufficient to measure anomaly contribution to g. Similar experiments continued during the next years with the aim to improve the precision of this measurement. The highest precision was obtained by Hutchinson and collaborators in 1963 [16] by stopping muons in a magnetic field and

---

[1]The meaning of A will be more clear in the next chapters.
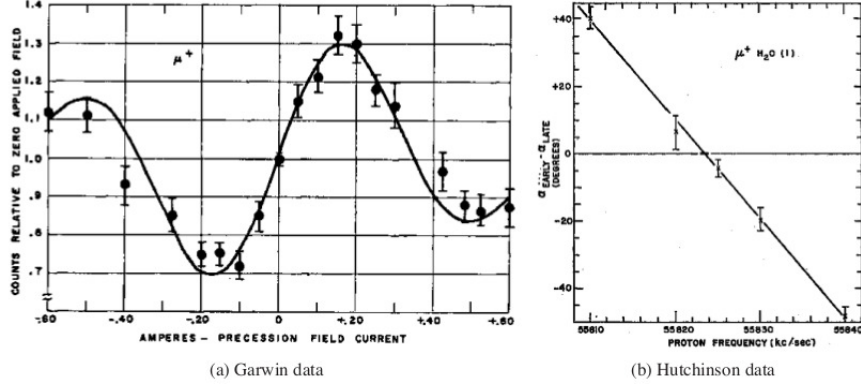
(a) Garwin data   (b) Hutchinson data

Figure 2.1: Historical plots showing Larmor precession data from the Garwin (a) and Hutchinson (b) experiments used to determine the muon *g-factor*.

measuring the early-to late phase difference between a standard reference and peaks in the decay electron distribution (Eq. 2.1). In Fig. 2.1 (b) it is shown the final result of the measurement of the Larmor precession frequency plotting the phase difference at a fixed time interval as a function of the reference clock and fitting for the zero crossing. In this experiment the magnetic field was measured via nuclear magnetic resonance (NMR) in terms of the Larmor precession frequency of protons in a polarized water sample, so it easier to express the results as a ratio λ of the two frequencies or magnetic moments obtaining

$$\lambda = \frac{\omega_\mu}{\omega_p} = \frac{\mu_\mu}{\mu_p} = 3.18338(4). \tag{2.3}$$

Using this result is possible to obtain a direct test with the QED prediction from Eq. 2.2.

2.2 The CERN experiments

Before Hutchinson published his results on the Larmor precession frequency a new experimental procedure was studied at CERN to increase the precision of the g-2 measurement, following the principles used in the determination of the electron's anomalous magnetic moment [17]. A charged particle moving in a uniform magnetic field B it will execute a circular motion with a cyclotron frequency

$$\omega_c = \frac{eB}{mc}. \tag{2.4}$$

It appears clear that taking the ratio between ω_s/ω_c the spin precession of muons moving into this magnetic field develops $1 + a_\mu$ times faster than the momentum vector. Taking the difference between the two frequencies the result is the *anomalous precession frequency* defined as

$$\omega_a = \omega_s - \omega_c, \tag{2.5}$$
$$= \frac{eB}{mc}\left(\frac{g}{2} - 1\right),$$
$$= \frac{eB}{mc}\frac{g-2}{2},$$
$$= a_\mu\frac{eB}{mc},$$

which is proportional to a_μ. Uncertainties on a_μ incorporate uncertainties on the magnetic field determination or in the muon mass determination but because $a_\mu \sim 1/800$ of g, measuring directly the anomaly increase the precision of almost three order of magnitude.

Looking at Fig. 2.2 it is possible to understand the spin precession concept. The figure shows the spin and momentum vectors for an initially forward polarized muon beam, moving along a circular orbit in a magnetic field. If
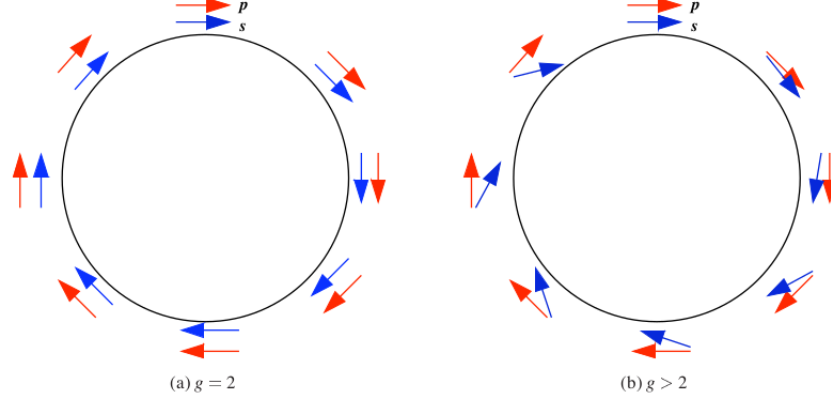
Figure 2.2: Illustration of the muon spin and momentum vectors for a muon orbiting in a magnetic field when $g = 2$ (a) and $g > 2$ (b).

the value of g is exactly 2, the situation is the one of the left panel, where the spin vector is locked to the momentum direction. Since g is a little larger than 2, the spin vector slightly rotates more than 2π during each cyclotron period, as shown on the right panel. This procedure developed at CERN permits to improve the experimental precision and from this concept a series of experiments with increasing precision came out; three were performed at CERN, which will be referred to as CERN I, CERN II and CERN III, one at the Brookhaven National Laboratory (BNL) and a new one is in construction at Fermilab (FNAL).

2.2.1 The CERN I experiment

In the first experiment at CERN a forward polarized muon beam is injected into a 6 m long magnet, with a magnetic field of 1.5 T. The magnetic field causes the muon beam to move in a spiraling orbit. To create this kind of motion is important to shim carefully the magnetic field in order to be parabolic in the vertical direction

$$B(y) = B_0(1 + ay + by^2), \qquad (2.6)$$

where the radius of the orbit is determined by the value of B_0, the linear term a causes each orbit to advance along the magnet and the term b produces a quadratic field providing vertical focusing. Increasing gradually the value of a increases the step size of orbital 'walking'. At the end of the magnet this gradient is large enough to allow the muons to escape from the field. A methylene-iodide target stops the beam and from the asymmetry of the decay electrons the polarization is extracted. To determine the spin precession relative to the momentum is necessary to determine the amount of time spent by the muon beam in the magnetic field. To avoid the use of a forward and backward detector, with different efficiencies for each, the magnetic field is pulsed to alternately rotate the muon spin by $\pm 90°$ before injection. Data from CERN I don't appear to be more precise than Garwin data, as shown in Fig. 2.3, but they represent a direct measurement of the anomaly. Therefore, the precision of 5×10^{-3} on a_μ

$$a_\mu^{exp}(1965) = 0.001162(5) \rightarrow 4300 ppm, \qquad (2.7)$$

implies a precision of 5 ppm on the determination of g.

The muon mass and the constants in Eq. 2.2 were known at the time of the CERN I experiment with an adequate precision to extract a_μ. But using different techniques for extracting a_μ like Hutchinson's, provide a measurement independent on the muon mass. This technique gains importance as the precision of the anomalous precession experiments improves, since Eqs. 2.2 can be written as

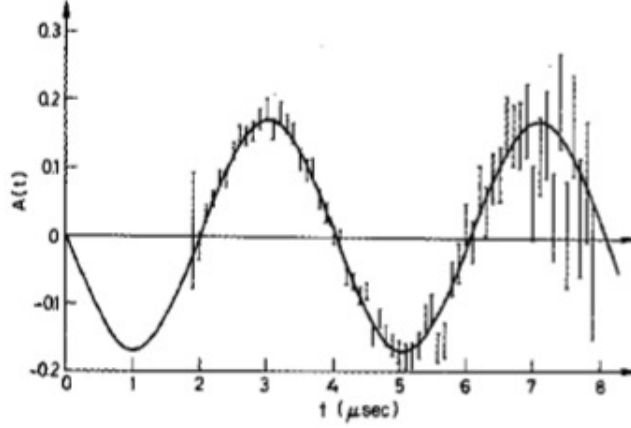$$\frac{\omega_a}{\omega_s} = \frac{a_\mu}{a_\mu + 1}. \qquad (2.8)$$

Figure 2.3: CERN I data.

Multiplying and dividing the left side of the equation for the Larmor precession frequency of proton ω_p in the same magnetic field, the ratio can also be written as

$$\frac{\omega_a}{\omega_s} = \frac{\omega_a \omega_p}{\omega_p \omega_s} \qquad (2.9)$$

The factor ω_p/ω_s in Eq. 2.9 is the inverse of the ratio λ (Eq. 2.3) measured by Hutchinson independently. Frequencies in numerator and denominator of Eq.2.9 are individually B dependent, but the ratio is not. This permits to take the value of λ and the ratio $\Re = \omega_a/\omega_p$ from different experiments to extract the value of a_μ. In fact solving Eq. 2.9 for a_μ considering λ and $\Re$ one obtains

$$a_\mu = \frac{\Re}{\lambda - \Re} \qquad (2.10)$$

With an accurate knowledge of λ, the value of a_μ can be extracted from experiments which measure the anomalous precession frequency ω_a and the proton Larmor frequency ω_p in the same apparatus. CERN I results were surprising due to the agreement with the prediction for the electron (see

Eqs. 1.3, 2.7). It was expected a noticeable deviation because of the moun mass, as in the proton and neutron case, but the result was the proof that in terms of QED the muon behaves just as an heavier electron. This result, together with the idea of a CERN II experiment, led theorists to improve the QED calculation to second order in α, with the new result [18]

$$a_\mu^{theor}(1965) = 0.00116552(5) \to \pm 42 ppm, \qquad (2.11)$$

where the error of 5×10^{-8} is due to the uncertainty in the virtual loops containing hadronic processes. This value can be improved to 1×10^{-8} with a first estimation of a third order QED calculation and by the knowledge of α. Uncertainties in the result of the CERN I experiment are mainly statistical. Examining the five parameter function Eq. 2.1 used to fit data, the fractional error on ω_a is [19]

$$\frac{\delta\omega_a}{\omega_a} = \frac{\sqrt{2}}{\omega_a A\tau\sqrt{N}}. \qquad (2.12)$$

To improve the accuracy the first option is to increase N; a second option is related to ω_a, which being proportional to the magnetic field, contributes increasing the number of cycle to be fit increasing the field strength; a third option is to use a more energetic muon beam with a bigger lifetime; the fourth option is to improve the asymmetry A of the signal with better detectors and a more accurate choice of the energy threshold to maximize the level of the parity violating decay electrons. The advent of the PS at CERN provided a more energetic muon source with a luminosity higher than the Synchro-cyclotron giving the idea to the same group of physicist of CERN I to exploit the possibility to perform a measurement of a_μ.
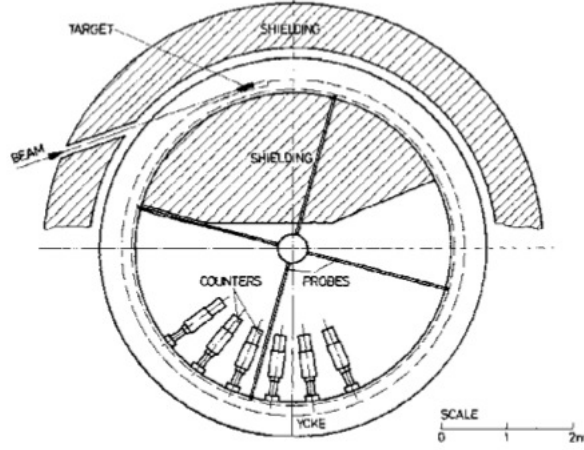
Figure 2.4: CERN II setup.

2.2.2   The CERN II experiment

To setup the CERN II experiment a 5 m diameter storage ring with a C-shaped cross section was built. The polarized muon source was obtained by injecting a 10.5 GeV proton beam against a target placed inside the storage ring. The 1.7 T field in the storage ring selects forward-going pions of momentum p = 1.27 GeV/c. As the pion decays, a beam of longitudinally polarized muons with a relativistic factor $\gamma = 12$ were captured in the storage ring. This injection process was inefficient creating a large background due to protons and the large amount of pion momenta produced a less than optimal initial muon polarization. However, the luminosity of PS and the factor 12 in the dilated lifetime more than CERN I made up for the inadequacies associated with the injection. The decay electrons from the stored muons bend radially inward with respect to the muon orbit because of their lower momentum. Therefore, detectors had to be placed around the inner radius of the ring to detect the decayed electrons. In Fig. 2.4 the experimental setup is shown.
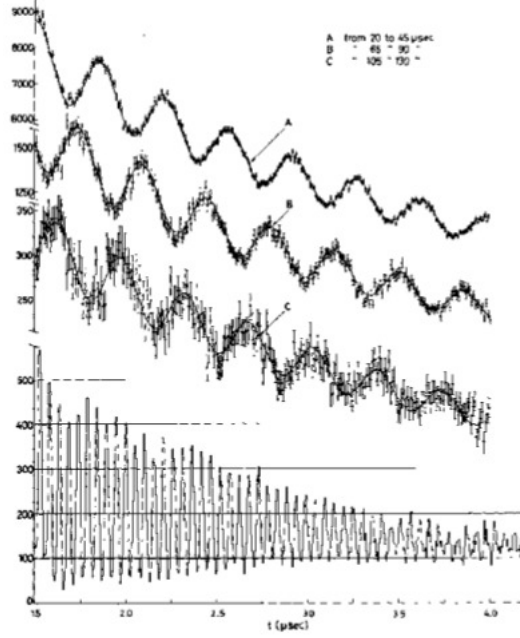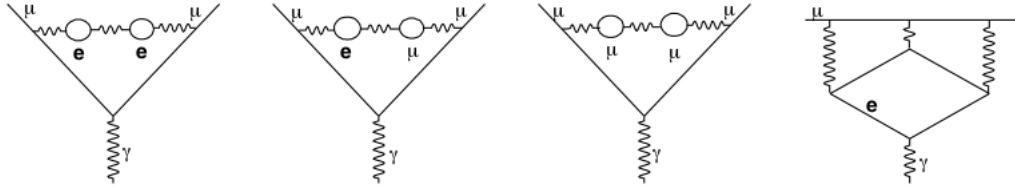
Figure 2.5: CERN II data.

Figure 2.6: Feynman diagrams for the 3rd order QED calculation.

The CERN II experiments was able to measure for a_μ (Fig. 2.5)

$$a_\mu^{exp}(1968) = 0.00116616(31) \rightarrow \pm 270 ppm, \qquad (2.13)$$

which is almost 2σ from the theoretical prediction. This level of discrepancy between the two values was resolved by Aldins and collaborators [21] examining QED contribution arising from light-by-light scattering Fig. 2.6. This contribution was assumed to be negligible but in 1969, was confirmed a 200 ppm contribution to the theoretical value of a_μ leading to a new

determination:

$$a_\mu^{theor}(1969) = 0.0116587(3) \rightarrow \pm 25 ppm, \tag{2.14}$$

confirming the agreement between the experimental and theoretical values. The increasing precision of the experimental procedure required to start considering the hadronic contributions to vacuum polarization in the theoretical calculation of a_μ. Quantum chromodynamics does not provide a method to calculate hadronic loops at low energies. A way out is to take the electromagnetic coupling of hadrons from experimental data using the dispersion relation [24]

$$a_\mu^{HVP} = \frac{1}{3}(\frac{\alpha}{\pi})^2 \int_{4m_\pi^2}^\infty \frac{R(s)}{s} K(s) ds, \tag{2.15}$$

where $R(s)$ is given by:

$$R(s) = \frac{\sigma(e^+e^- \rightarrow hadrons)}{\sigma(e^+e^- \rightarrow \mu^+\mu^-)} \tag{2.16}$$

and the fucntion $K(s)$ is the QED kernel function. A more precise determination of the cross section data obtained at Novosibirsk and Orsay [22, 23] experiments, were included as first in the paper of Gourdin and de Rafael [24], where they present a contribution to a_μ of $65.(0.5) \times 10^{-8}$ with the error calculated solely from the uncertainty in the cross section measurements. At this point from the experimental point of view physicists started again to search a way to improve the precision of the measurements considering that the CERN II experiments ended with a statistical error of 2.3×10^{-7} and a systematic error of 1.9×10^{-7}

2.2.3 The CERN III experiment

The systematic uncertainty coming from the CERN II experiment is entirely due to the radial variation in the magnetic field required to provide vertical confinement. A possible solution could be to use a quadrupole electric field to prevent the stored muons from oscillateing up and down into the magnet yoke. A relativistic muon will see this quadrupole electric field in the lab frame as a magnetic field in its rest frame; so the anomalous precession frequency will be derived as

$$\vec{\omega_a} = \frac{e}{m} \left[a_\mu \vec{B} - \left(a_\mu - \frac{1}{\gamma^2 - 1} \right) (\vec{\beta} \times \vec{E}) \right].$$ (2.17)

As can be seen from Eq. 2.17 the last term introduces a dependence of the spin frequency on the electric field; while NMR probes provides an extremely precise way to determine the magnetic field, there's no way to measure electric field at the same level of precision. Even if the option of electric quadrupoles seems not a practicable option, if the coefficient in front of the term $(\vec{\beta} \times \vec{E})$ can be made zero the measurement of the electric field is not required. It comes out that for the correct relativistic enhancement

$$\gamma = \sqrt{\frac{1}{a_\mu} + 1}$$ (2.18)

this coefficient is precisely zero. The related muon momentum[2] p_μ is 3.09 GeV/c which corresponds to a momentum easily reachable at the PS. For the goals established for the CERN III the Hutchinson error of 13 ppm in the determination of λ was not sufficient anymore, so most scientist undertook the endeavor to have a better λ measurement, with the most precise determination obtained by Ken Crowe and collaborators [25]

---

[2]Called magic momentum p.

$$\lambda = \frac{\omega_\mu}{\omega_p} = \frac{\mu_\mu}{\mu_p} = 3.1833467(82). \tag{2.19}$$

Once these major problems were solved the CERN III experiment began. The experience obtained with CERN II was used to revisit the whole scheme and improve the experimental setup:

- background was reduced by not injecting protons directly into the ring, but placing the target outside and using an inflector to inject pions into the storage region. This allowed also to place detectors all around the circumference, increasing statistics, because the shielding block were not necessary as in CERN II.

- using a beamline to transport pions permitted to select a very narrow range of pion momenta increasing the polarization of stored muons;

- the magic momentum meant that the relativistic lifetime of the muons is precisely 64.4 μs, which is more than a factor of two larger than CERN II.

As we can see by analyzing these points almost all the factors in the denominator of Eq. 2.12 were improved as can be seen easily from Fig. 2.7. The final result obtained after combining data for both positive and negative muon was

$$a_\mu^{exp}(1979) = 0.001165924(8.5) \rightarrow \pm 7ppm, \tag{2.20}$$

where the fact that the 7 ppm error is dominated by statistical uncertainty proved the robustness of the new magic momentum technique. With a total uncertainty in theoretical prediction of 11 ppm the CERN III results did not discover the origin of the muon mass but proved the importance of the hadronic vacuum polarization contribution to the 5σ level.
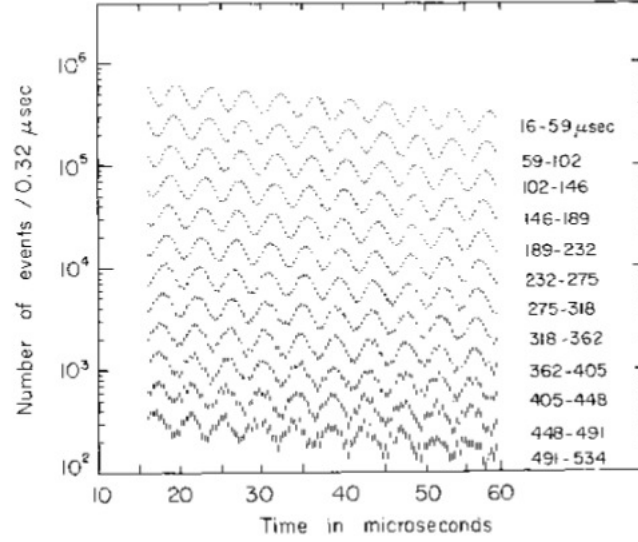
Figure 2.7: CERN III data. As can be easily seen the wiggles are visible up to 500 μs w.r.t the CERN II data of Fig. 2.5 which are up to 130 μs.

2.3 The Brookhaven experiment

After the CERN III result, the theoretical progress on the determination of a_μ slowed down to the point that an immediate experiment pushing forward the precision was no longer justifiable. It was only after the calculation of the α^4 order QED term by Kinoshita and collaborators [26] and improvements on the measurement of $R(s)$ cross sections in the hadronic sector, that a group of physicist of the CERN experiments started to think about a possible experiment to be performed at the Alternate Gradient Synchrotron (AGS) at BNL. Despite the 4 ppb precision of the electron g-2 experiments at that time the sensitivity to heavy particles due to the muon with respect of electrons compensate adequately the factor 100 in precision. Thanks to this reason an experiment to measure a_μ to 0.35 ppm was established at BNL. The experimental method of the storage ring was not yet exhausted so the

first step of the experiment was to reach a factor 20^3 of overall improvement with respect to the CERN III. A first factor comes from the AGS itself which is capable of delivering a beam which is almost a factor 20 more intense than the PS at CERN; the second step comes from a better method of injection. In the CERN experiments a flux of pion was injected inside the storage ring and the decaying muons were captured while for this experiment was found that let decay the pions outside the storage ring and injecting the resulting muon beam increase the flux dramatically. To avoid interference of this muon beam with the inflector magnet after the first orbit a series of kicker should be implemented shifting the muon orbit after injection.

Together with this, are listed below some other improvements on the systematics effects:

- the storage ring is constructed with three continuously wound superconductors, as opposed to the series of 40 independent conventional bending magnets used in CERN III;

- the inflector incorporates a superconducting shield to minimize the disruption of the field in the storage region, and unlike the CERN inflector, allows it to operate in DC mode;

- a NMR system capable of making *in situ* measurement of the field in the storage ring was designed, which unlike CERN III, does not require cycling the magnet power;

- in the BNL experiment, the decay electron signals from the calorimeters are recorded by waveform digitizers and stored for later analysis instead of relying on a hardware trigger.

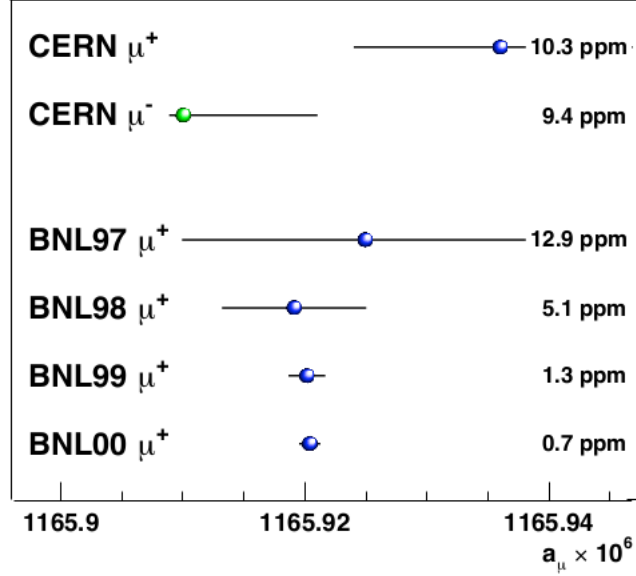---

[3]A factor 400 in the muon flux.

Figure 2.8: Progression of the experimental precision from CERN through the 2000 BNL data set.

It took almost 15 year of developments before starting data taking in 1997, and the first years of runs were just some test of the new improvements and subsystems. Nevertheless they were useful and gave also interesting results as shown in Fig. 2.8.

In the years 1999 and 2000 data on the positive muon were taken obtaining a precision on a_μ of 0.7 ppm (Fig. 2.9) and then was decided to switch to the negative muon.

The switching procedure was a success and combining data from both measurement the BNL experiment ended with a total result of [27]

$$a_\mu = 11659208(6) \times 10^{-10}[0.54ppm], \tag{2.21}$$

That resulted in a difference with the theoretical value of the time of 2.7σ.
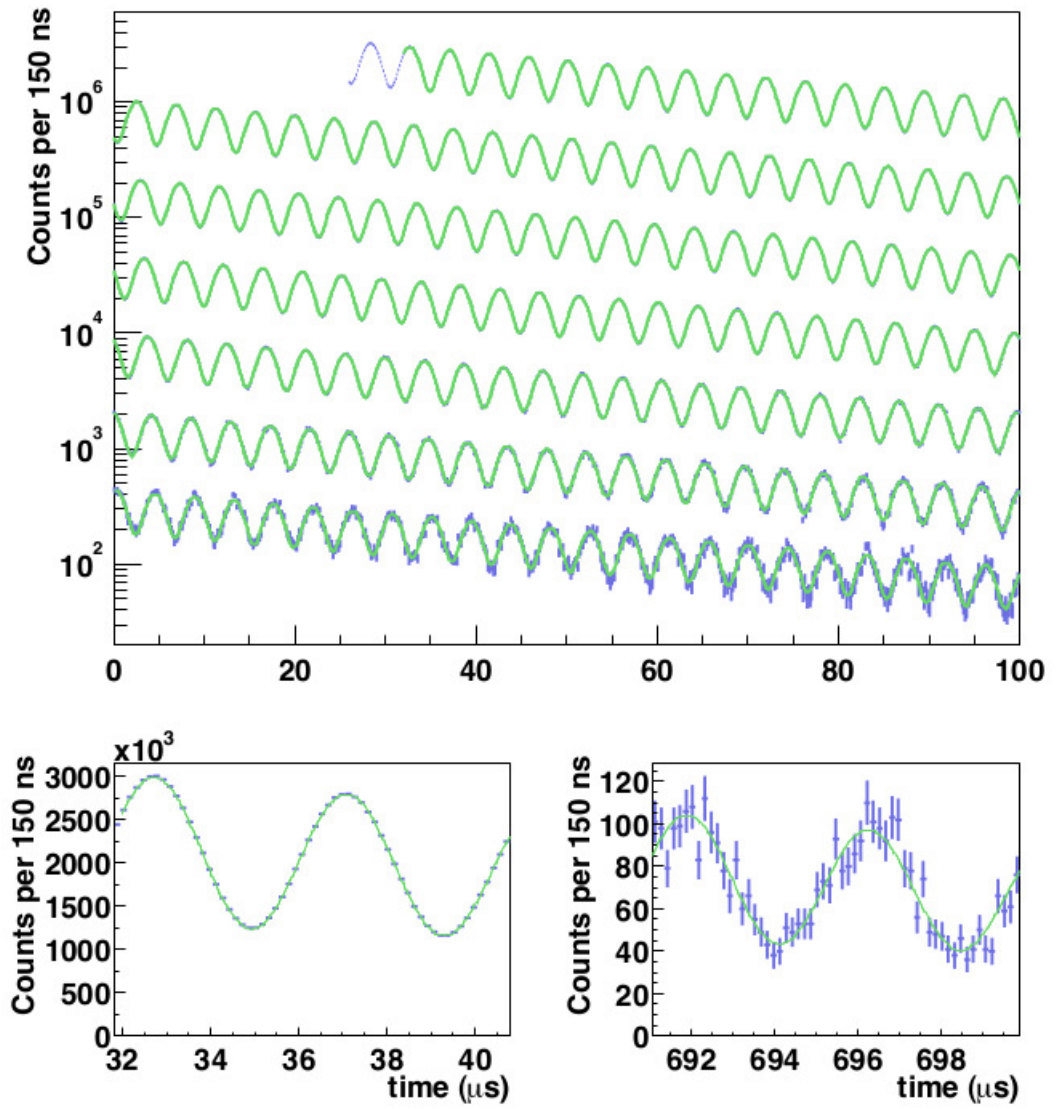
Figure 2.9: Decay electron data from 2000 positive muon data set. As can be seen easily with respect to Fig. 2.7 the improved statistics make the signal clearly visible up to 700 μs.

Chapter 3

Standard Model Calculation of the muon g-2

3.1 Overview of the calculation

The current prediction of a_μ with the given level of accuracy arises from the contribution of different sectors of quantum field theory, i.e quantum electrodynamics (QED), electroweak theory (EW) and quantum chromodynamics (QCD). For this reason is useful to split a_μ^{SM} into these contributions

$$a_\mu^{SM} = a_\mu^{QED} + a_\mu^{EW} + a_\mu^{HVP} + a_\mu^{HLbL} \tag{3.1}$$

where a_μ^{HVP} and a_μ^{HLbL} are the QCD contribution and one refer to them as hadronic vacuum polarization and hadronic light by light respectively.

In Table 3.1 a summary of the contributions of each term is also indicated. Although the dominant contribution comes by far by QED, the error on the Standard Model comes entirely from the hadronic terms as can be seen from Table 3.1.

	Value $(\times 10^{-11})$
a_μ^{QED}	116584718.95±0.08
a_μ^{EW}	154 ±1
a_μ^{HLbL}	105 ±26
a_μ^{HVP}(lo) [34]	6923 ± 42
a_μ^{HVP}(lo)	6949 [35]± 43
a_μ^{HVP}(ho) [35]	-98.4 ± 0.7
Total SM [34]	$116591802 \pm 42_{H-LO} \pm 26_{H-HO} \pm 2_{other} \ (\pm 49_{tot})$
Total SM [35]	$116591828 \pm 43_{H-LO} \pm 26_{H-HO} \pm 2_{other} \ (\pm 50_{tot})$

Table 3.1: Standard model contribution to a_μ.

3.2 QED contribution

The QED contribution has been calculated up to terms of order α^5 yielding [28],

$$\alpha_\mu^{QED} = \frac{\alpha}{2\pi} + 0.765857425(17)(\frac{\alpha}{2\pi})^2 + 24.05050996(32)(\frac{\alpha}{2\pi})^3+$$
$$+130.8796(63)(\frac{\alpha}{2\pi})^4 + 753.3(1.0)(\frac{\alpha}{2\pi})^5 = 116584718.95(0.08) \times 10^{-11} \quad (3.2)$$

where the small error results mainly from the uncertainty in α. The value of α^{-1} used for this calculation is

$$\alpha^{-1} = 137.035999049(90) \quad (3.3)$$

obtained [29] from the precise measurement of the recoil velocity of Rubidium h/m_{Rb} [30], the Rydberg constant and m_{Rb}/m_e [29]
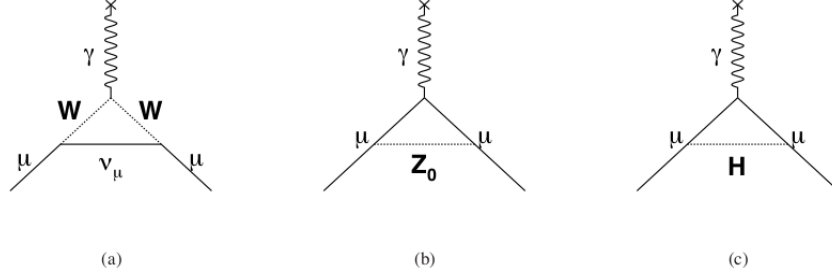
Figure 3.1: Contributions to a_μ from the weak sector arise from diagrams containing (a) a $W^\pm$, (b) Z, or (c) a Higgs exchange.

3.3 The EW contribution

The contribution from the EW sector is dominated by diagrams containing a virtual exchange of a $W^\pm$,Z, or a Higgs boson, see Fig. 3.1

The single loop contribution was calculated by several authors starting from Jackiw and Weinberg in 1972 [31]. The final calculations yields

$$a_\mu^{EW}(1-loop) = \frac{5G_F m_\mu^2}{24\sqrt{2}\pi^2}\left[1 + \frac{1}{5}(1 - 4\sin^2\theta_W)^2 + O(\frac{m_\mu^2}{M_{Z,W,H}^2})\right] = 194.8\times10^{-11}$$

(3.4)

This term enters with a suppression of $(m_\mu/M_W)^2$ related to the W contribution with respect to the QED calculation and introduces a perturbation of approximately 3.3 ppm. The single loop Z-exchange reduces the overall EW contribution with a negative fractional value of -1.6 ppm while the single-loop Higgs contribution has an additional suppression of $(m_\mu/M_W)^2$ not contributing significantly to the single-loop calculation. Taking into account also higher order contributions to the EW sector [32] the final value is $a_\mu^{EW} = 153.6(1) \times 10^{-11}$ considering the Higgs mass $M_H = 125.6(1.5)$ GeV where the error comes from hadronic loop uncertainties and 3-loop non leading logs.
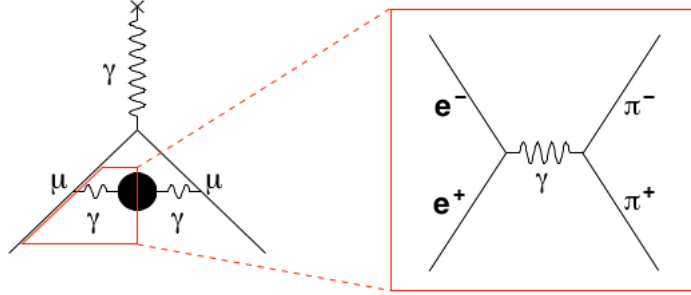
Figure 3.2: Feynman diagrams on the left shows the lowest-order HVP, where the "blob" in the middle indicates any possible contribution of quarks. This contribution can be related to the cross section for hadron production.

3.4 The hadronic contribution

The hadronic contribution has been the subject of intense theoretical work over the last several years. Since it dominates the uncertainty on a_μ with a contribution of about 60 ppm, improvements in this sector are crucial. Because of the non-perturbative nature of QCD at low energies, the hadronic contributions cannot be calculated from first principles. Focusing first on the HVP, it can be calculated from $e^+ e^-$ annihilation into hadron final states data, using the dispersion relation of Eq.2.15

where R(s) comes from Eq. 2.16. This relation can be demonstrated by considering Fig. 3.2 where the box around the photon propagator in the Feynman diagram on the left can be related to the diagram corresponding to $e^+e^- \to \pi^+\pi^-$ production on the right[1]. This intermediate hadronic state is the dominant contribution, but for a full estimate all possible hadronic states must be considered.

In addition to the factor $1/s$ in the integrand of Eq. 2.15, the QED kernel K(s) also approximately scales as $1/s$. Therefore, the integral is heavily

---

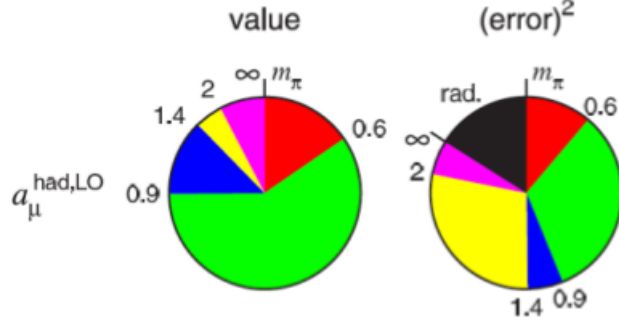[1]The $\pi^+\pi^-$ production channel is one of the possible channels.

Figure 3.3: Contributions to the dispersion integral for different energy regions and to the associated error squared on the dispersion integral in that region. Taken from ref.[35].

weighted towards low mass energies in the region of the ρ resonance; however at the level of precision needed, data up to 2 GeV become important. Fig.3.3 shows the contribution to the integral for the different energy regions on the left, and the contribution to the error squared on the right.

In the last years several determination where obtained for the hadronic vacuum polarization which used the same data set with different data treatment, see Figs. 3.4, 3.5

$$a_\mu^{HVP} = 6923(42)_{tot} \times 10^{-11}[34] \tag{3.5}$$

$$a_\mu^{HVP} = 6949(43)_{tot} \times 10^{-11}[35] \tag{3.6}$$

The contribution to a_μ from higher-order loops hadronic diagrams is calculated to be [35]

$$a_\mu^{HOHVP} = (-98.4 \pm 06_{exp} \pm 0.4_{rad}) \times 10^{-11} \tag{3.7}$$

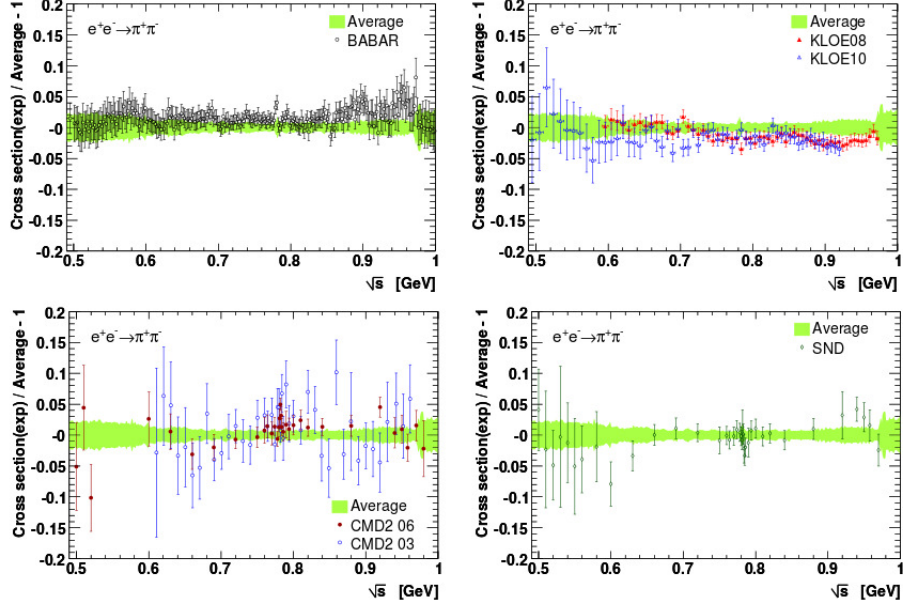The calculation needed to obtain this result is similar to the first-order HVP,

Figure 3.4: Comparison between individual $e^+e^- \to \pi^+\pi^-$ cross sections measurement from BABAR, KLOE08, KLOE10, CMD2 03. CMD2 06, SND and the HVP-Tools average. The error bars shows statistical and systematic errors added in quadrature. Taken from Ref. [34]
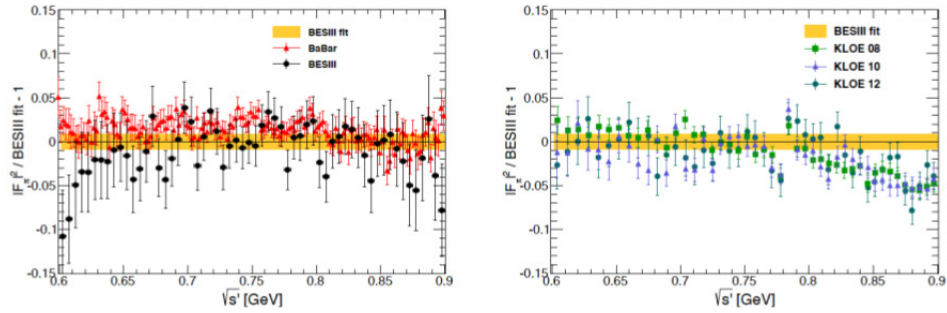

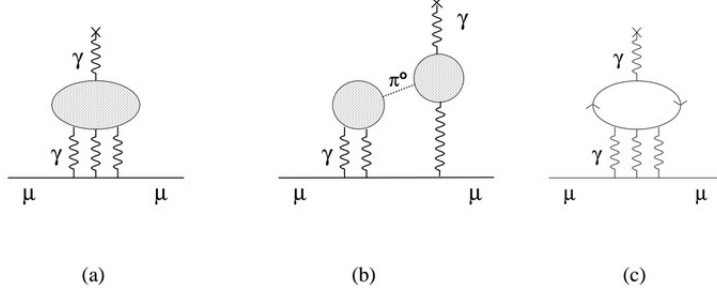Figure 3.5: Recent results from BESIII collaboration [37]

Figure 3.6: Feynman diagrams for (a) the general case of hadronic light-by-light scattering, (b) interaction involving two three-point loops connected by exchange of a pseudoscalar such as π^0, and (c) four-point loop interaction, where the particle in the loop may be a free quark or a meson.

so it requires also the experimental input from R(s)

$$a_\mu^{HVP} = \frac{1}{3}(\frac{\alpha}{\pi})^2 \int_{4m_\pi^2}^\infty \frac{R(s)}{s} K^2(s) ds, \tag{3.8}$$

and knowledge of the Kernel $K^2(s)$ for higher-order loops [38]. Overall, the error on the calculation on HOHVP is small compared to the first order term. This term includes all higher-order hadronic contributions, except for a special class of interactions known as hadronic light-by-light (HLbL) scattering Fig. 3.6. The main difference between the HLbL term and the HVP is that light-by-light scattering cannot be related to experiment, so it must be estimated from theoretical principles through different models. Prior to 2001 this term was thought to be about -8×10^{-10}. But it was found out that a mistake in two independent calculation resulted in a sign error. A synthesis of the model contributions, which was agreed upon authors working in this field, known as the Glasgow Consensus, can be found in [41]

$$a_\mu^{HLbL} = +105(26) \times 10^{-11} [41] \tag{3.9}$$

A different evaluation [33] leads to a same central value but with a larger uncertainty (102 ± 39).

3.5 The standard model prediction for a_μ

Combining all various contributions explained in the previous sections the total prediction for the muon anomalous magnetic moment can be summarized as

$$a_\mu^{SM} = (116591802 \pm 49) \times 10^{-11}[34] \tag{3.10}$$

$$a_\mu^{SM} = (116591828 \pm 50) \times 10^{-11}[35] \tag{3.11}$$

where the different evaluations come from two different groups.

3.6 Possible new physics scenario.

The theoretical work is still ongoing in the evaluation of a_μ together with experimental effort to improve the measurement of the anomalous magnetic moment of the muon. This effort could lead to a discrepancy between the theoretical value and the experimental one larger than 5σ, with the E989 experiment entering the game. If such a discrepancy is obtained which could be the explanation if due to new physics?

3.6.1 Muon compositeness

The vast spectrum of hadrons is explained by the quark model; in the same way, fundamental "preons"[42] might be able to account for the existence of
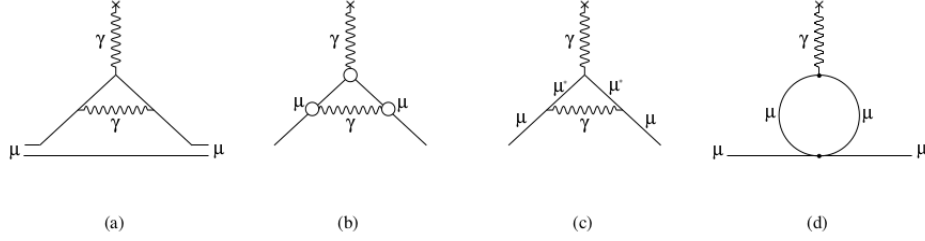
Figure 3.7: Feynman diagrams [43] for (a) the leading-order effect of compositeness, which must be canceled out in a workable model; (b) a form factor at each $\mu\gamma$ interaction vertex; (c) exited lepton states; (d) four fermion contact interactions.

multiple generations of leptons. As already said in chapter 1 the magnetic moment of proton and neutron is dramatically different from 2 because they are composed of quark; it could be expected that a perturbation to a_μ is due to some constituents of the muon. An initial model is represented by the tree-level Feynman diagram in Fig. 3.7 (a).

The associated contribution to a_μ is linear [44] in the ratio of the muon mass to the characteristic scale $\Lambda = \frac{1}{r}$. Unfortunately, models with such a linear terms are untenable. Even the CERN III measurement of a_μ was sufficient to require $\Lambda > 2000$ TeV. Furthermore, the simple model leads to a self-energy term that would enhance the muon mass to an unphysical value. Any reasonable compositeness model must be constructed to cancel out these effects. One natural way to achieve this cancellation is to build a chirally symmetric wavefunction in which the left-handed and right-handed interaction terms exactly balance [44].

Once the linear contribution has been removed, substructure affects a_μ in three ways. First, each vertex at which a muon interacts with another particle is multiplied by a form factor $(1 + \frac{q^2}{\Lambda^2})$ to account for the spatial extent of the charge distribution. Second, the muon may enter excited states

in which the constituents have acquired relative orbital angular momentum. Finally, there may be contact interactions among the constituents that do not correspond to the usual exchange of gauge bosons. Feynman diagrams representative of each of these categories are shown in Fig. 3.7 (b)-(d). The numerical results are clearly dependent on the details of the model; however, the contribution to a_μ is always proportional [43] to $(\frac{m_\mu}{\Lambda})^2$. Likely the order of the coefficients, after the summation of all the diagrams, is 1. Consequently,

$$a_\mu^\Lambda = O[(\frac{m_\mu}{\Lambda})^2],$$ (3.12)

a measurement of a_μ to 0.014 ppm is capable of constraining Λ at energies of the orders of TeV.

3.6.2 Supersymmetry

Inside the SM, masses of fundamental particles and couplings associated with interactions are free parameters, determined by spontaneous symmetry breaking . However, they appear conspiring to give a dramatic cancellation in their effects on the Higgs boson mass. This problem is known as the "gauge hierarchy problem". Each fermion f that couples directly to the Higgs causes a radiative correction to its mass of [45]

$$\Delta m_H^2 = \frac{|\lambda_f|^2}{16\pi^2} \left[-2\Lambda_{UV}^2 + 6m_f^2 \ln\left(\frac{\Lambda_{UV}}{m_f}\right) + ... \right].$$ (3.13)

The corresponding perturbation from a boson field S has a similar form, except for an opposite sign

$$\Delta m_H^2 = \frac{|\lambda_f|^2}{16\pi^2} \left[2\Lambda_{UV}^2 - 2m_S^2 \ln\left(\frac{\Lambda_{UV}}{m_S}\right) + ... \right].$$ (3.14)

Λ_{UV} is high-momentum cutoff parameter that regulates the integration, preventing divergence. It is expected to fall near the Planck scale $m_P = 2.4 \times 10^{18}$ GeV, causing tremendous corrections to m_H even if the couplings λ_f and λ_S are small. These corrections must be reduced by a very large factor because m_H is 125 GeV. It is possible that the contributions for fermions and bosons to cancel out spontaneously, but only with a very careful choice of their masses and couplings. A very unlikely event. Theory of supersymmetry provides a way to avoid this fine-tuning problem by postulating the existence of a symmetry between bosons and fermions; each boson has a fermion partner and viceversa. The theoretical motivation for supersymmetry is compelling, but still there is no experimental evidence for the partner particles. This symmetry must be broken by some "soft" terms to the Lagrangian otherwise masses of the various partners should be the same of the paired ones, which means that they should have been seen long time ago. This new partner particles are labeled using and *s*- as a prefix for fermions having *squarks* and *sleptons*; the suffix *-ino* is used for bosons: so photon becomes *photino* and so on. Another effects of supersymmetry is that this theory leads to two Higgs doublets: one gives mass to the upper half of each generation (u, c and t quarks) and the other gives mass to the lower half (d, s and b quarks). Of this four states, two are electrically neutral, one is positive and the other is negative. The ratio $tan\beta = \frac{v_2}{v_1}$ of the vacuum expectation values of the Higgs doublets is an important parameter describing the nature of supersymmetry and its scale is related to the ratio of top and bottom quark and is of the order of 40.

In Fig. 3.8 the lowest-order contribution to a_μ are shown. The first thing to note is that this contributions are identical to the dominant standard model electroweak contribution. The $\tilde{\mu}$ represent the smuon and the $\tilde{\nu}$ the
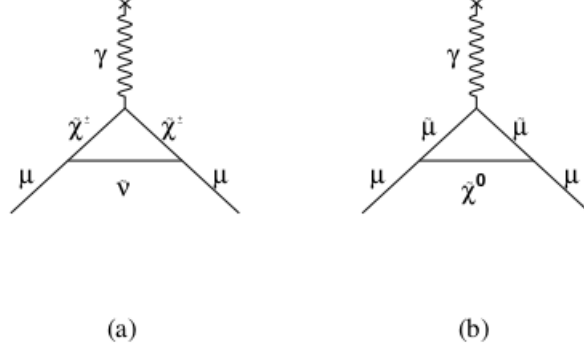
Figure 3.8: Feynman diagrams for the lowest-order supersymmetric contributions to a_μ.

sneutrinos. The $\tilde{\chi}^0$ and $\tilde{\chi}^\pm$ are called neutralino and chargino respectively: these are the mass eigenstates whose linear combinations give photino, wino, zino and Higgsinos which clearly here are not mass eigenstates.

One more realistic supersymmetric model does not assume to have degenerate masses. The Minimal Supersymmetric Standard Model (MSSM) describes a very general form of supersymmetric breaking. It has 105 independent parameters as masses, phases and mixing angles beyond those of the ordinary Standard Model [45]. But if we consider the leading contribution on a_μ only a small number of those parameters are involved in the calculation, which are listed below:

- $tan\beta$;

- M_1, M_2 and μ, the mass scales associated with the photino, wino/zino and Higgsino respectively;

- $m_{\tilde{\mu}_L}$ and $m_{\tilde{\mu}_R}$, the mass scales of the left-handed and right-handed sleptons;

- a_μ a parameter that describes the mixing of left and right-handed smuons.

This set of parameters can be reduced just postulating a mechanism responsible for supersymmetry breaking. As example, assuming unification with the gravitational force at the Planck scale, is possible to construct a supergravity model, in which only four relevant parameters remain [46].

3.6.3 Dark photon

A recent BSM scenario involves the so called "dark photon", an hypothetical relatively light vector boson from the dark matter sector that express its interaction with ordinary matter through mixing with the ordinary photon [47, 48]. The strength of the coupling expressed as $\epsilon \cdot e$, where ϵ is the kinetic mixing term between ordinary and dark photon, give rise to a contribution to a_μ:

$$a_\mu^{dp} = \frac{\alpha}{2\pi}\epsilon^2 F(m_V/m_\mu). \tag{3.15}$$

where the factor F is defined as

$$F(x) = \int_0^1 \frac{2z(1-z)^2}{[(1-z)^2 + x^2 z]dz}. \tag{3.16}$$

Taking $\epsilon \sim 1 - 2 \times 10^{-3}$ and $m_V \sim$10-100 MeV the dark photon can provide a viable solution to the muon g-2 discrepancy. All the dark sectors searches were originally motivated by cosmology. Searches for a dark photon in this mass range are currently underway at flavor factories and dedicated experiments at CERN (NA48 and NA62), the Jefferson Lab and MAMI in Mainz, and PADME in Frascati.

More new Physics

The BSM models presented in this chapter are not the only possible new physics scenario, but they were presented here as examples. There are much more possibilities including electric dipole moment, leptoquarks, compact extra dimension and so on. For further reading the reader is referred to [49].

Chapter 4

The E989 experiment at Fermilab

The error achieved by the BNL E821 experiment was $\delta a_\mu^{EXP} = 6.3 \times 10^{-10}$ (0.54 ppm). The greater than 3σ difference found by E821 with respect to the theoretical prediction, does not meet the 5σ threshold for claiming a discovery, so a more precise measurement was desirable.

The goal of the new g-2 experiment at Fermilab (E989) is a four-fold improvement in the experimental precision thereby reducing the error on the measurement of a_μ down to 0.14 ppm which should be compared to the 0.4 ppm uncertainty of the most accurate Standard Model prediction [50].

While BNL E821 improved on the CERN III experiment in a revolutionary manner, primarily by the invention of direct muon injection into the storage ring, the FNAL E989 experiment will introduce a broad suite of refinements focused on optimizing the beam purity and rate, the muon storage efficiency, and modernizing the instrumentation used to measure both ω_a and ω_p [51]. E989 will use the same muon storage ring of E821, which has been relocated to Fermilab in a new building characterized by mechanical stability and

controlled temperature. These options were not available at BNL [52]. The E989 experiment will measure a_{μ^+} during the first run, due to the enhanced cross section for producing π^+ at the target and due the fact that negative muons tend to be captured in matter more often than positive muons; a_{μ^-} could be measured in a second run. Measuring both signs provides a test of CPT theorem. Since the values measured for a_{μ^+} and a_{μ^-} in the E821 experiment were consistent, the E821 Collaboration averaged the two values to produce their final experimental value for a_μ [27]. The total uncertainty of 0.14 ppm expected for the E989 experiment is subdivided into 0.1_{stat} ppm + 0.1_{sist} ppm. The 0.1 ppm statistical uncertainty is a factor 21 improvement on muon rate with respect to the previous experiment. To reach this value the Fermilab accelerator complex permits to have:

- higher proton rate with less protons per bunch: the Fermilab beam complex which is expected to annually deliver $2.3 \cdot 10^{20}$ 8 GeV protons on an Inconel[1] core target; at this rate, the desired statistics of 1.8×10^{11} detected positrons with energy greater than 1.8 GeV, will be achieved in less than two years of running [52];

- 6-12 times larger muon yield per proton and a $\times 3$ fill higher rate; the muon storage ring will be filled at a repetition rate of 12 Hz, which is the average rate of muon spills that consists of sequences of successive 700 μs spills with 11 ms spill-separations, compared to 4.4 Hz at BNL [52];

The 0.1 ppm systematic uncertainty is also challenging and some specific improvements are:

---

[1]Inconel is an alloy, composed of a metal and other elements, specially designed to withstand high beam stresses.

- a longer pion decay line: a limiting factor at BNL was the 120 m beamline between the pion production target and the storage ring; because the decay length of a 3.11 GeV/c pion is $\approx$ 173 m, the beam injected into the storage ring contained both muons and a significant number of undecayed pions, the latter creating an enormous burst of neutrons when intercepting materials: their subsequent capture in scintillator-based detectors impacted detector performance adversely [51]; this background will be reduced by a factor of 20 in E989 due to a pion decay line of ~2000 m;

- improved detectors and new electronics: the detectors and electronics will all be newly constructed to meet the demands of measuring the anomalous spin precession frequency ω_a to the 0.07 ppm level; this is a substantial improvement over the E821 experiment where the total systematic error on ω_a was 0.18 ppm [50]. Better gain stability and corrections for overlapping events in the calorimeters are crucial improvements addressed in the new design.
  A new tracking system will allow for better monitoring the orbit of the stored muons, thus improving the convolution of the stored muon population with the magnetic field volume, and establishing corrections to ω_a that arise from electric field and pitch corrections, which are related to vertical particle oscillations (pitch effect): the vertical undulation of the muons means $\mathbf{p_\mu}$ is not exactly perpendicular to $\mathbf{B}$, thus a small "pitch" correction is necessary at the current and proposed levels of experimental precision [54];

- better shimming to reduce B-field variations: the storage ring magnetic field, and thus ω_p, will be measured with an uncertainty of 0.07 ppm,

ω_a			ω_p		
Category	E821 [ppb]	E989 [ppb]	Category	E821 [ppb]	E989 [ppb]
Gain changes	120	20	Absolute field calibration	50	35
Pileup	80	40	Trolley probe calibrations	90	30
Lost muons	90	20	Trolley measurements of B_0	50	30
CBO	70	<30	Fixed probe interpolation	70	30
E and pitch	50	30	Muon distribution	30	10
			Time dependent external B fields	-	5
			Others[2]	100	30
Total	180	70	Total	170	70

Table 4.1: Total systematics error on ω_a and ω_p of E821 and expected values of E989.

that is approximately 2.5 times smaller by placing critical Nuclear Magnetic Resonance (NMR) probes at strategic locations around the ring and shimming the magnetic field to achieve a high uniformity, in addition to other incremental adjustments [55];

- a continuous monitoring and re-calibration of the detectors, whose response may vary on both the short timescale of a single fill, and the long time scale of an entire run, will be required: a high-precision laser calibration system that will monitor the gain fluctuations of the calorimeter photodetectors at 0.04 % accuracy will be used [53].

4.1 Review of the experimental technique

The experimental technique was briefly presented in Chapter 2 following the historical development of the experiment. Here a more focused and detailed description is given.

The concept of the measurement is the following: injecting a beam of polarized muons into a uniform magnetic field and measure the rate at which the spin process with respect to the momentum $\vec{\omega_a} = \vec{\omega_S} - \vec{\omega_C}$, where $\vec{\omega_S}$ and $\vec{\omega_C}$ stands for the spin precession frequency and the cyclotron frequency. In absence of any external fields the spin and cyclotron frequencies are given by:

$$\omega_S = -g\frac{Qe}{2m}B - (1-\gamma)\frac{Qe}{\gamma m}B; \tag{4.1}$$

$$\omega_C = -\frac{Qe}{\gamma m}B. \tag{4.2}$$

As a result the difference ω_a is

$$\omega_a = \omega_S - \omega_C = -(\frac{g-2}{2})\frac{Qe}{m}B = -a_\mu\frac{Qe}{m}B, \tag{4.3}$$

which is the same as Eq. 2.2. From this simple equations is important to note two features which makes the experiment work:

- ω_a depends on the anomaly and not on the full magnetic moment;

- it depends linearly on the magnetic field.

From these two simple considerations it follows that to determine the anomaly, is necessary to measure only ω_a and the magnetic field B. Actually the quantity that is relevant is the average of B over the muon distribution, $\langle B \rangle$ [50],

$$\langle B \rangle = \int M(r,\theta)B(r,\theta)rdrd\theta \tag{4.4}$$

where $B(r,\theta)$ and $M(r,\theta)$ are expressed respectively as

$$B(r,\theta) = \sum_{m=0}^{\infty} r^n(c_n\cos n\theta + s_n\sin n\theta), \tag{4.5}$$

$$M(r,\theta) = \sum_{m=0}^{\infty} (\xi_m(r) \cos m\theta + \sigma_m(r) \sin m\theta). \qquad (4.6)$$

The harmonic terms in Eqs. 4.5, 4.6 are orthogonal terms, it means they vanish for each term with $n \neq m$, so the only contribution is for products of the same moment/multipole. The way to determine the value of $\langle B \rangle$ to ppm precision is to have a very excellent knowledge of all the moments and multipole distributions or to take care to minimize the number of terms participating, making the first term to be large, in order to have just a few multipoles contributing. Actually the second option is the one adopted. This option obviously seems to forbid any kind of confinement and vertical focusing of the muon beam because no magnetic gradients are permitted. In the presence of E field, a relativistic particle feels a motional magnetic field proportional to $\vec{\beta} \times \vec{E}$, changing Eq. 4.3 to [56, 57]:

$$\vec{\omega_a} = -\frac{Qe}{m} \left[a_\mu \vec{B} - \left(a_\mu - \frac{1}{\gamma^2 - 1} \right) \frac{\vec{\beta} \times \vec{E}}{c} \right]. \qquad (4.7)$$

Fortunately working with a momentum of 3.09 GeV, the *magic momentum*, the second term vanishes and no electric field contributes to the beam motion, making the measurement possible. The same treatment could be done if the possibility to have an Electric Dipole Moment of the muon (EDM)[3] is taken into account. The net effect of an EDM is to tip the plane of polarization precession out of the ring plane by the angle $\delta = \tan^{-1} \frac{\eta\beta}{2a_\mu}$[4] and increase the magnitude of the precession frequency according to $\omega = \sqrt{\omega_a^2 + \omega_\eta^2}$. One of the features of the E989 experiment is that it will be equipped with three tracking stations that are useful for determining the properties of the stored muon beam, having the up-down oscillating EDM

---

[3]A possible new physics effect.

[4]The symbol η plays the same role for EDM as g plays for the magnetic moment.

signal for free. The experiment should be able to improve the muon EDM limit with respect to E821 [58]

$$d_\mu < 1.8 \times 10^{-19} e \cdot cm (95\% CL). \tag{4.8}$$

of two or more orders of magnitude.

The way to measure ω_a is related to the muon decay properties. The dominant muon decay mode is

$$\mu^\mp \to e^\mp + \nu_\mu(\bar{\nu}_\mu) + \bar{\nu}_e(\nu_e) \tag{4.9}$$

which violates parity. The muon beam is produced from a beam of pions which traverse a straight beam channel constituted by a set of focusing and defocusing elements (FODO), selecting the forward an backward decay in order to ensure polarization. The experiment uses forward muons which are the one produced with the highest laboratory momenta. Their polarization is directed along (μ^-) or opposite (μ^+) their laboratory momenta. The (V-A) three body weak decay of the muon provides information on the muon spin orientation thanks to a correlation between the decay of high energy electrons[5] and the spin itself. Taking the approximation that the energy of the decay electron $E' >> m_e c^2$ the differential decay distribution is given by [59]

$$dP(y', \theta') \propto n'(y')[1 \pm A(y') \cos\theta']dy'd\Omega' \tag{4.10}$$

where $y' = p'_e/p'_{emax}$, $d\Omega'$ is the solid angle and θ' is the angle between the muon spin and $\vec{p}'_e$. This definition is valid until we refer to the muon rest frame. Moving to the laboratory frame we can have directly the electron

---

[5]The word electron will be used both for electron and positron in this section.

(a) No detector acceptance or energy resolution included

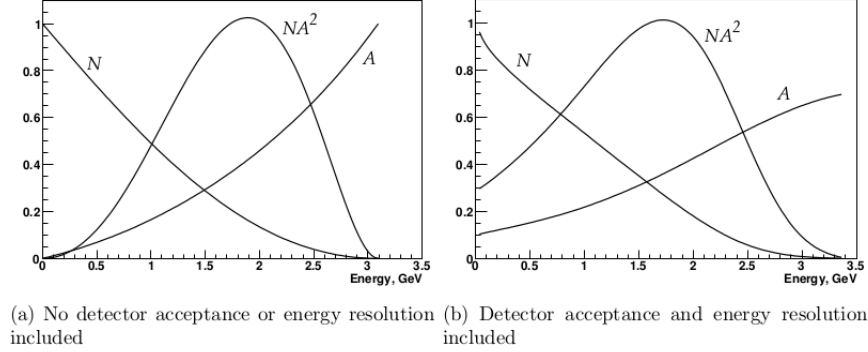(b) Detector acceptance and energy resolution included

Figure 4.1: The integral N, A, and NA^2 in arbitrary units for a single energy-threshold as a function of the threshold energy in the laboratory frame. a) Not including the detector acceptance and energy resolution of the E821 experiment; b) including all this effects.

oscillation number as a function of the emitted electron energy above the energy threshold

$$N(t, E_{th}) = N_0(E_{th}) \exp^{-\frac{t}{\tau_\mu}} [1 + A(E_{th}) \cos(\omega_a t + \phi(E_{th}))]. \qquad (4.11)$$

Eq. 4.11 is the same of Eq. 2.1. As already discussed N is the number of electrons, N_0 the number of electrons at t=0, A is the asymmetry, τ_μ is the muon dilated life time and ϕ is the phase.

In Fig. 4.1 is shown the statistical figure of merit (FOM) NA^2 according to Eq. 2.12 together with the distribution for N and A.

The energy threshold is needed because if *all* the decay electrons are counted, the number detected as a function of time will be a purely exponential; therefore it is important to apply cut on the energy in the laboratory frame in order to select only the electrons emitted in the same direction as the muon spin, it means the ones whose number oscillates at the precession frequency, which are the most energetic ones. The value of the

energy threshold comes directly maximizing the FOM and is ~ 1.8 GeV. The decay electrons have a smaller momenta than the muon parents, curling inward and going out the magic orbit being detected from the various calorimeter stations placed around the storage ring.

Besides the measurement of ω_a it is important to measure the magnetic field through the frequency ω_p. To obtain a_μ we use Eq. 2.10 which requires precise knowledge of the muon mass.

4.2 Experimental apparatus

The experiment is based on the following 8 points:

1. Production of an appropriate pulsed proton beam by an accelerator complex.

2. Production of pions using the proton beam that has been prepared.

3. Collection of polarized muons from pion decay $\pi^+ \to \mu^+ \nu_\mu$.

4. Transporting the muon beam to the g-2 storage ring.

5. Injection of the muon beam into the storage ring.

6. Kicking the muon beam onto storage orbits.

7. Measuring the arrival time and energy of positrons from the decay $\mu^+ \to e^+ \bar{\nu}_\mu \nu_e$.

8. Precise mapping and monitoring of the precision magnetic field.

4.2.1 Production and injection of the Muon beam

The E989 experiment will bring a bunched beam from the 8 GeV Booster to a pion production target located where the antiproton production target was during Tevatron runs. Pions of 3.11 GeV/c $\pm$ 5% will be collected and sent into a large-acceptance beamline. Muons [6] are produced in the weak pion decay

$$\pi^+ \to \mu^+ + \nu_\mu. \tag{4.12}$$

The neutrino is left-handed and the pion is spin zero. Thus the muon spin must be anti-parallel to the neutrino spin, so it is also left-handed. A beam of polarized muons can be obtained from a beam of pions by selecting the highest-energy muons or lowest-energy muons, obtaining a beam with a polarization greater than 90%. Pions and daughter muons will be injected into the Delivery Ring, where after several turns the remaining pions decay. The pion decay line is $\sim$2 km long while the one of Brookhaven was only 120 m. The surviving muon beam will be extracted and brought to the muon storage ring built for E821 at Brookhaven in Fig. 4.2.

The storage ring magnet is energized by three superconducting coils. The continuous "C" magnet yoke is built from twelve 30° segments of iron, which were designed to eliminate the end effects present in lumped magnets. This construction eliminates the large gradients that would make a precision determination of the average magnetic field $\langle B \rangle$ very difficult. Furthermore, a small perturbation in the yoke can affect the field at the ppm level at the opposite side of the ring. Thus every effort is made to minimize holes in the yoke, and other perturbations. The only penetrations to the yoke are to

---

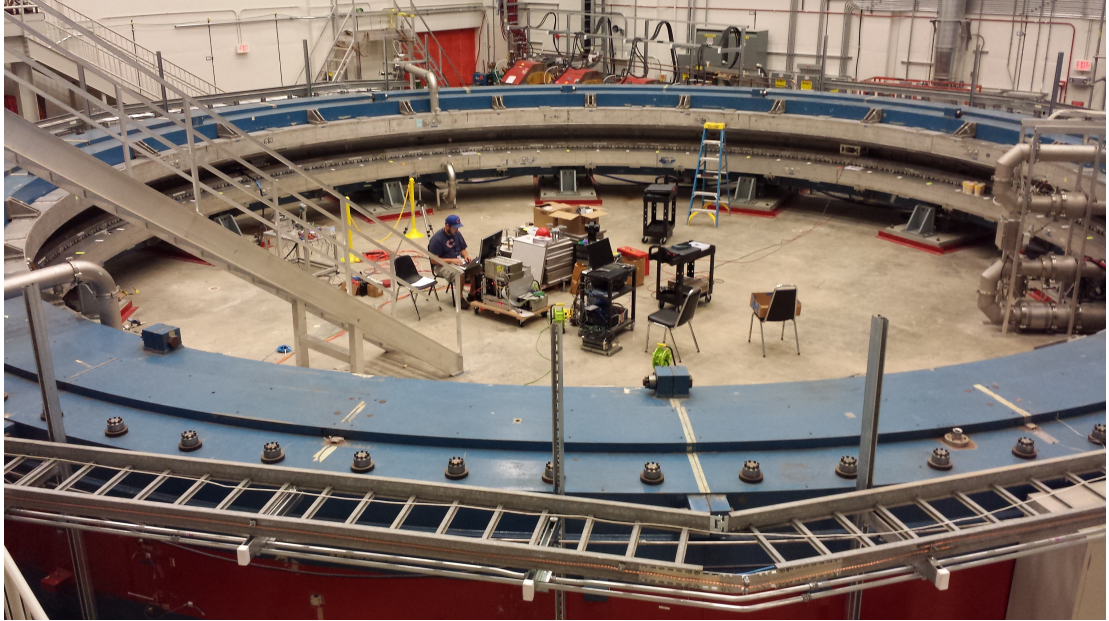[6]The term muon is used in general for muons and also for anti-muons.

Figure 4.2: The E821 ring magnet in the MC-1 building at Fermilab. Courtesy of Fermi National Accelerator Laboratory.

permit the muon beam to enter the magnet as shown in Fig. 4.3 (a), and to connect cryogenic services and power to the inflector [50] magnet and the outer radius coil, Fig. 4.3 (b).

The beam enters through a hole in the "back-leg" of the magnet and then crosses into the inflector magnet, which provides an almost field free region, delivering the beam to the edge of the storage region. Once that the beam is injected it requires to be kicked otherwise it will impact against the inflector after one turn. The kick required to put magic momentum muons onto a stable orbit centered at the magic radius is on the order of 10 mrad. There are strictly requirements on the muon kicker:

1. Since the magnet is continuous, any kicker device has to be inside the precision magnetic field region.
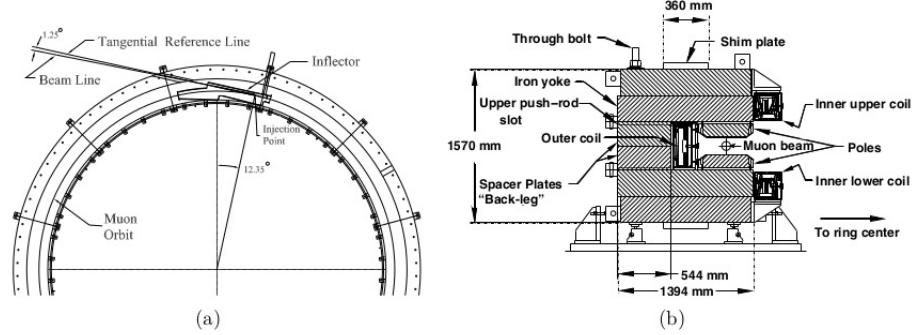
Figure 4.3: (a) Plan view of the beam entering the storage ring. (b) View of the storage ring cross section.

2. The kicker hardware cannot contain magnetic elements such as ferrite, because they will affect the precision uniform magnetic field.

3. Any eddy currents produced in the vacuum chamber, or in the kicker electrodes by the kicker pulse must be negligible by 10 to 20 μs after injection, or must be well known and corrected for in the measurement.

4. Any kicker hardware has to fit within the real estate that was occupied by the E821 kicker. The available space consists of three consecutive 1.7 m long spaces.

5. The kicker pulse should be shorter than the cyclotron period of 149 ns.

4.2.2 Detector system

The detector system of the E989 experiment consists of 24 calorimeter stations along the inner radius of the storage ring. Differently from the E821 experiment, where each calorimeter was made of 4 monolithic block of PbW/SciFi readout by PMTs through light guides, this experiment has a block of 54 PbF_2 crystals, 6 height by 9 wide, readout by fast large area silicon-photomultipliers (SiPM). Each crystal is a $2.5 \times 2.5 \times 14$ cm^3 pure

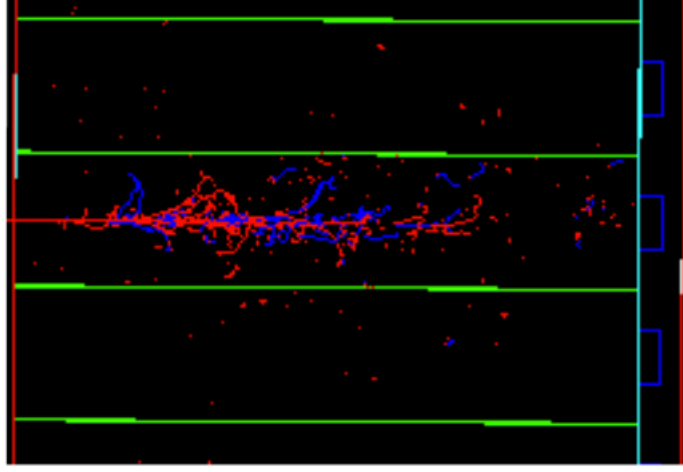Figure 4.4: A single shower showing secondary positrons (blue) and electrons (red) in a $2.5 \times 2.5 \times 14$ cm^3 PbF$_2$ crystal, subject to a 2 GeV positron incident on the left.

Cerenkov with a density of 7.77 g/cm^3. The 14 cm length corresponds to $15X_0$ radiation lengths with a Moliére radius of 2.2 cm. The choice of a pure Cerenkov material is driven by the almost instantaneous signal produced when an electron strikes a crystal. This improves a lot the time resolution of the experiment also contributing to pile-up events recognition. Pile-up recognition is also improved thanks to high granularity of the calorimeter. The PbF$_2$ crystals have a very low magnetic susceptibility, perfect for working in a magnetic environment without perturbing the magnetic field itself. Several test beams have been performed[7] to verify all the properties of the crystals together with an intense simulation work, see for example Fig. 4.4. One of the result of the test performed on the crystals was the choice of the wrapping material. The wrapping that will be used is a black-tedlar absorptive material which, even if it has a light yield lower than a reflective

---

[7]Some of them will be described in the last chapter of this Thesis.

Crystal cross section	2.5×2.5 cm^2
Crystal length	14 cm ($> 15X_0$)
Array configuration	6 rows, 9 columns
Density of material	7.77 g/cm^3
Magnetic susceptibility	-58.1$\times 10^{-6}$ cm^3/mol
Radiation length	0.93 cm
Moliére radius R_M	2.2 cm
Moliére R_M (Cerenkov only)	1.8 cm
$E_{threshold}$ for Cerenkov light	102 keV

Table 4.2: Properties of led fluoride crystals.

one, ensures a faster response of the crystal to a radiation. In Tab. 4.2 a summary of crystal properties is available [50].

The fast nature of these crystals will be useless if not coupled with an appropriate photo-detector. SiPMs satisfy all the requirements needed for the experiment. SiPM works as a pixelated Geiger-mode counter, with 57600 50 μm-pitch pixels on a 1.2×1.2 cm^2 device. Quenching resistors are intrinsic to the device to arrest the avalanche and allow the device to recover with a recovery rime constant typically of 10's ns. The selection of SiPMs over PMTs is pragmatic. They can be placed inside the storage ring fringe field without perturbation, avoiding the long light guides that would be needed for remote PMTs as in E821. They have also an high-photodetection efficiency and can be mounted directly to the rear face of the PbF$_2$ crystals. Another aspect is that these device are cheaper than same size-PMTs. Some of the challenging features of SiPM are their high sensitivity to temperature and bias voltage. The calorimeter design is prepared to handle the

temperature dependence together with temperature control of the MC-1[8] building. Regarding bias voltage control a custom low-voltage power supply will be used with a 1 mV accuracy. Each power supply will serve 5-6 SiPM in order to minimize common fluctuation of all the 1300 due to bias voltage. To ensure the high level of stability requested for the experiment a high performance calibration system is required for the on-line monitoring of the output stability of each individual calorimeter station. All the 1300 channel must be calibrated during data taking and the proposed solution is based on the method of sending simultaneous light calibration pulses close as much as possible to the signal produced by a positron, directly to the photo-detectors through the active sections of the calorimeter. More detail about this calibration system will be discussed in the next Chapter.

4.2.3   Magnetic field

The high level of precision needed to determine a_μ reflects on the determination of ω_a and $\langle B \rangle$. The muon beam once injected is confined to a cylindrical region with a radius of 9 cm and 44.7 m in length. The scale for the magnetic field measurement and its control is set by the total volume of this region which is ~ 1.14 m^3. The goal of the experiment is to know the magnetic field averaged over time and the muon distribution to an uncertainty of $\pm\, 0.07$ ppm.
This problem can be divided into 5 different aspects:

1. Producing as uniform magnetic field as possible by shimming the magnet.

---

[8]The MC-1 is the building where the experiment will be housed.

2. Stabilizing B in time at the sub-ppm level by feedback, with mechanical and thermal stability.

3. Monitoring B to 20 ppb level at the storage ring during data collection.

4. Periodically mapping the field throughout the storage region and correlating the field map to the monitoring information without turning off the magnet between data collection and field mapping. It is essential to not turn off the magnet unless it is absolutely necessary.

5. Obtaining an absolute calibration of the B field relative to Larmor frequency of the free proton.

There is only one possibility to measure the magnetic field to the required accuracy by using nuclear magnetic resonance (NMR) as in E821 experiment. The measurement in the E989 experiment is done using a $\pi/2$ RF pulse to rotate the proton spin and then the resulting free-induction decay will be detected by a pick-up coil around the sample. There are three different kind of probes: a spherical water probe that provides the absolute calibration to the free proton; cylindrical probes that monitor the field during data collection, and also in an NMR trolley to map the field; a smaller spherical probe which can be plunged into the muon storage region by means of a bellows system to transfer the absolute calibration to the trolley probes. A collection of 378 cylindrical probes placed in symmetrically machined grooves on the top and bottom of the muon beam vacuum chamber provide a point-to-point measure of the magnetic field while beam is in the storage ring. Probes at the same azimuthal location but different radii gave information on changes to the quadrupole component of the field at that location.

The field mapping trolley contains 17 cylindrical probes arranged in concentric circles as shown in Fig. 4.5 (a). Every 2-3 days during the running
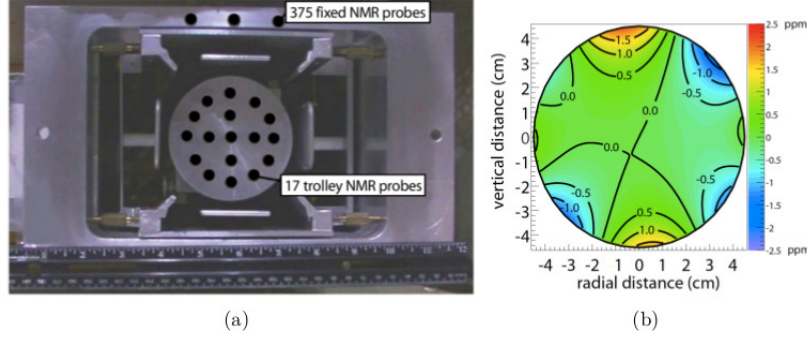
Figure 4.5: (a) The electrostatic quadrupole assembly inside a vacuum chamber showing the NMR trolley sitting on the rails of the cage assembly. Seventeen NMR probes are located just behind the front face in the places indicated by the black circles. The inner (outer) circle of probes has a diameter of 3.5 cm (7 cm) at the probe centers. The storage region has a diameter of 9 cm. The vertical location of three of the 180 upper fixed probes is also shown. Additional 180 probes are located symmetrically below the vacuum chamber. (Copyright 2006 by the American Physical Society.) (b) A contour plot of the magnetic field averaged over azimuth, 0.5 ppm intervals.

periods, the beam will be turned off, and the field mapping trolley will be driven around the inside of the evacuated beam chamber measuring the magnetic field with each of the 17 trolley probes at 6000 location around the ring. One of the resulting E821 field maps, averaged over azimuth, is shown in Fig. 4.5 (b).

The absolute calibration uses a probe with a spherical water sample [60]. The Larmor frequency of a proton in a spherical water sample is related to that of the free proton through [61, 62]

$$\omega_L(sph - H_2O, T) = [1 - \sigma(H_2O, T)]\omega_L(free) \tag{4.13}$$

where $\sigma(H_2O, 34.7°C)$=25.790(14) $\times 10^{-6}$ comes from the diamagnetic

shielding of the proton in the water molecule, determined in Ref. [63].
An alternate absolute calibration explored for the E989 experiment consist of
an optically pumped ^{3}He NMR probe [64]. This solution has several
advantages: the sensitivity to the probe shape is negligible and also the
temperature dependence is negligible. Test on the different solution will be
performed to choose the best option.

Chapter 5

Laser Calibration System

The goal of the E989 experiment is to measure the muon anomaly with a total error of 0.14 ppm. To reach this level of accuracy lessons from the BNL experiment will be used to improve the experimental technique and the experimental setup as described in the previous chapter. The laser calibration system is one of these improvements; its task is to monitor the gain fluctuations of the photodetectors (SiPM) allowing for a total systematic uncertainty of 0.02 ppm as described in Tab. 5.1. The system should be able to monitor any fluctuation inside the muon fill time window (700 μs).

5.1 Physics motivation

The importance of the laser calibration system is related to the response of the photodetectors. Its task is to control gain fluctuations allowing for a maximum systematic error of 0.02 ppm as shown in Tab. 5.1

Ideally the gain function should be $G(t) = 1$ at all times. If the possibility to have small gain changes is taken into account the fluctuations is simply defined as $\Delta G(t) = G(t) - 1$; this possible fluctuation affects each parameter

E821 Error	Size[ppm]	Plan for E989 experiment	Goal[ppm]
Gain changes	0.12	Better laser calibration and low-energy threshold	0.02
Lost muons	0.09	Long beam line eliminates non-standard muons	0.02
Pileup	0.08	Low energy samples recorded; calorimeter segmentation	0.04
CBO	0.07	New scraping scheme; damping scheme implemented	0.04
E and pitch	0.05	Improved measurement with traceback	0.03
Total	0.18	Quadrature sum	0.07

Table 5.1: Comparison of the E821 systematic errors with the requirements for the E989 experiment.

of Eq. 2.1: in fact with a first order Taylor expansion

$$N(t) = N_0(1 + \left(\frac{1}{N}\frac{dN}{dG} \right) \Delta G(t)) \tag{5.1}$$

$$NA(t) = NA_0(1 + \left(\frac{1}{NA}\frac{d(NA)}{dG} \right) \Delta G(t)) \tag{5.2}$$

$$\Delta\phi(t) = \frac{d\phi}{dG}\Delta G(t) \tag{5.3}$$

Following the previous equations is clear that each possible gain drift should be corrected because affects directly the parameters of the fit function used to obtain ω_a from the data set. A high performance calibration system is required for the on-line monitoring of the output of each calorimeter station.

5.1.1 Gain Fluctuations studies

To estimate the effects of the gain fluctuations, a set of known functions have been considered when fitting the "wiggle-plot". In this approach, the first step is to create the unperturbed data set, which consist of the simulated
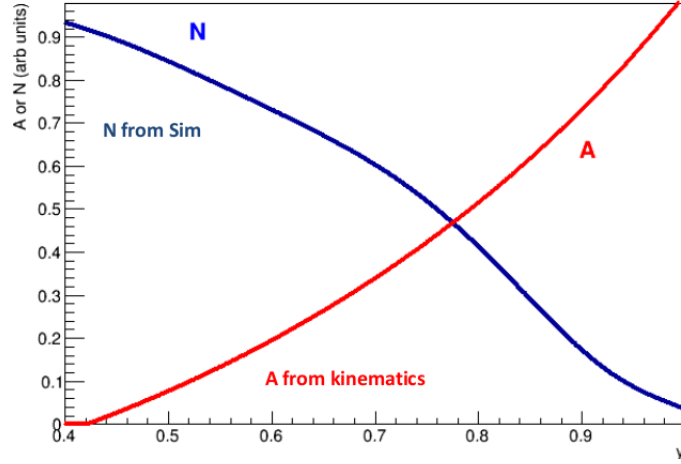
Figure 5.1: Theoretical functions (normalized to 1) of N(y) and the asymmetry A(y) versus the normalized energy of the e^-.

total data plotted, without any drift or gain fluctuations effects, considering detector acceptance, resolution and statistical fluctuations. To put it as an histogram in bin of 149 ns[1] a technique called "Layer Cake technique" is used. It consists in building the wiggle plot from layers of energy from y=y_{tresh} to y=1[2]; for each layer of width dy the theoretical function of N(y) and A(y) and ϕ(y) are shown in Fig. 5.1 and Fig. 5.2. It is also important to take into account energy resolution of the detector, assigning a proper weight to each energy layer. In this way a probability matrix for each energy layer can be built as shown in Fig. 5.3.

With all these parameters the wiggle plot can be built and fitted with Eq. 2.1 to extract the unperturbed value for ω_a Fig. 5.4. The gain fluctuation is then included, by shifting the observed value of the normalized energy y according to the time dependence of the perturbation.

---

[1]It represents the cyclotron time.

[2]The normalized energy y is defined as the ratio of the energy of the electron/positron E to the maximum energy E_{max} $y = \frac{E}{E_{max}}$ ($E_{max} = 3.1$ GeV/c).
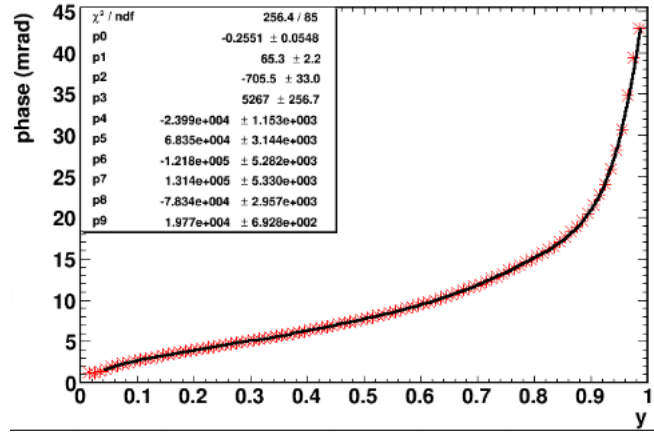
Figure 5.2: $\phi(y)$ as obtained by a polynomial fit of the drift time of the decaying electrons.
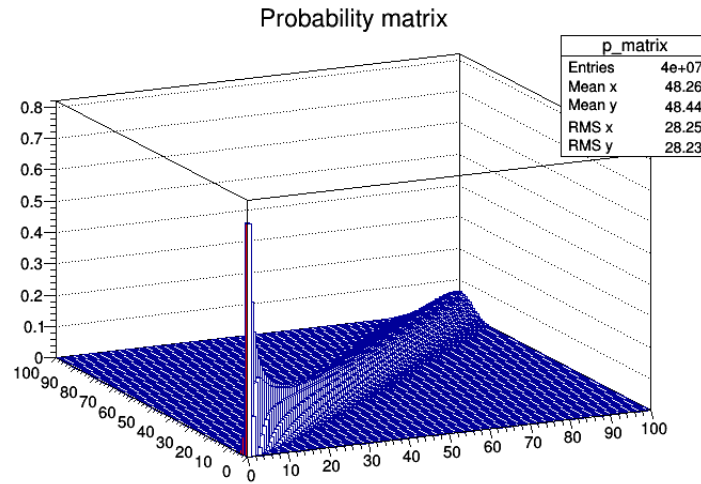

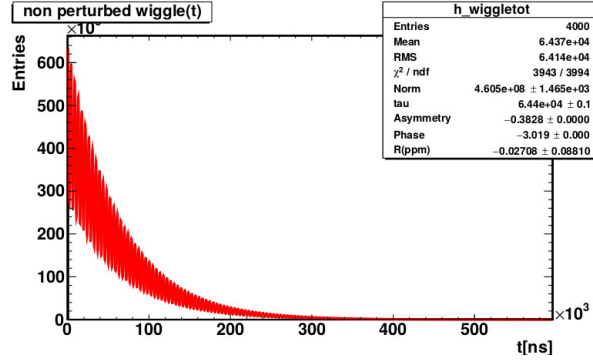Figure 5.3: Detector resolution matrix relating E measured vs E true.

Figure 5.4: Unperturbed wiggle plot in the time window 0-700μs considering the total data set of 1.8×10^{11} positron collected by the experiment. This plot is built applying an energy threshold y_{tresh}=0.6, or E_{tresh}=1.8 GeV, and a bin width = 149 ns. The function used to fit the wiggle plot is the usual 5 parameter function $N(t) = N(y)e^{-t/\tau}([1 + Acos(\omega_a(1 + R)t + \phi(y))]$. The parameter extracted from the fit is R which is the fractional difference from the nominal value of ω_a in the unperturbed state.

The time dependence of the gain fluctuations has been parametrized by the following functions:

1. linear drift: $G(t)=1 + \epsilon(t_{end}-t)/t_{end}$, (where $t_{end} = 700$ μs);

2. exponential drift due to rate variation: $G(t)=1+\epsilon e^{-t/\tau}$;

3. periodical drift due to the spin precession: $G(t)=1+\epsilon cos(\omega_a t + \phi)$.

In Tab. 5.2 the results of this study are shown. It is important to keep in mind that the maximum source of fluctuation allowed is 0.02 ppm. The statistical error of 0.08 is the one expected with the full data set.
In Fig. 5.5 values vs the magnitude of the fluctuations (ϵ parameter) for the different functions are shown with the 20 ppb maximum allowed region. Until the perturbation remains inside this region no laser corrections are needed. However the real function of gain fluctuations is a priori unknown

G(t) function	$\epsilon(10^{-3})$	χ^2/Ndf	R[ppm]
1	0	0.98	-0.02 ± 0.08
Linear(1)	1	1.16	-0.03 ± 0.08
Linear(1)	5	5.05	-0.08 ± 0.08
Exponential(2)	1	9.1	0.36 ± 0.08
Cosine(3) $\phi = \pi$	1	1.6	-0.02 ± 0.08
Cosine(3) $\phi = \pi/2$	1	1.6	-0.04 ± 0.08
Cosine(3) $\phi = \pi$	5	15.5	-0.02 ± 0.08
Cosine(3) $\phi = \pi/2$	5	15.5	-0.13 ± 0.09

Table 5.2: Results for stable and perturbed case for three sets of function with different magnitude. The maximum fluctuation permitted after correction is 0.02 ppm.

and is important to recognize and correct any source of fluctuation outside the safe region of the 20 ppb area.

5.2   Distribution System

Almost 1300 channels must be calibrated during data taking; the proposed solution is based on the method of sending simultaneous light calibration pulses through the crystals to the photodetectors. These light pulses must be stable in intensity and timing to correct for systematic effects due to drifts in the response of the crystal readout devices. Moreover a suitable photodetector system should be included in the calibration system to monitor any possible fluctuation in time and intensity of the calibration light source due to: intensity and beam pointing fluctuation of the source, fluctuation or changes of the transmitted light fraction along the optical path
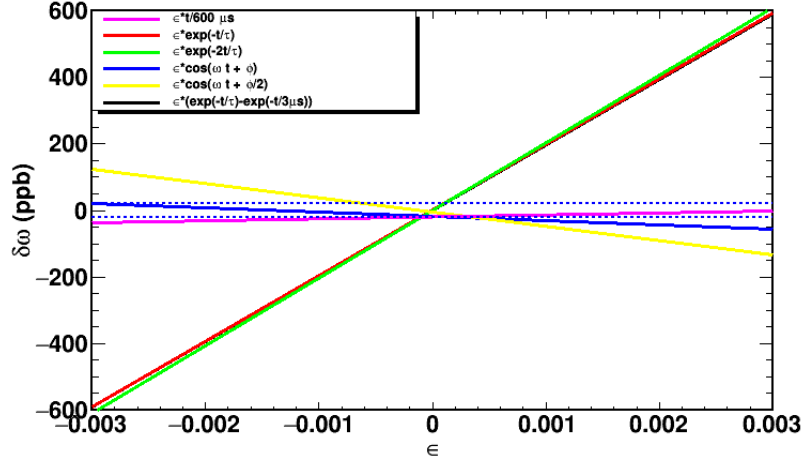
Figure 5.5: $\Delta\omega_a$ variation with respect to ϵ for the different set of functions used for this study. The 2 horizontal lines delimit the "safe" 20 ppb zone where perturbation are below the systematic error value set for the experiment.

of the light distribution system, mechanical vibrations and aging of the optics. The choice of the best light source and the design of the laser calibration system architecture are based on some guidelines. For the light source the following criteria were used [50]

- light wavelength must be in the spectral range accepted by the detector and determined by the convolution of the spectral density of the Cerenkov signal produced by electrons in PbF_2 crystals with the spectral transmission of the crystals, and with the spectral Q.E. of the photodetector;

- the luminous energy of the calibration pulses must be in the range of the electron deposit in the crystal, typically 1-2 GeV; this corresponds to a luminous energy on each tower of about 0.01 pJ at 2 GeV;

- the pulse shape and time width must be suitable to infer on the

readout capability in pile-up event discrimination; pulse rise/trailing time must be of the order of some hundreds of picoseconds, the total pulse width should not exceed 1 ns. This implies a peak power per pulse at the source of some Watts, assuming the conservative value $0.001 < T < 0.01$ for the total intensity transmission factor of the laser calibration system;

- the pulse repetition rate must be of the order of 10 kHz; this value is obtained searching the best compromise between the need of having enough calibration statistics and the need to avoid saturation of the DAQ bandwidth and perturbation of data due to the laser pulses. If necessary this value can be tuned to improve this optimization.

Among the different laser types, those that better fit the above mentioned requirements are pulsed diode laser systems at 405 nm. They also offer the important capability of being externally triggered in a very wide range of rates. This option is very important to reproduce the real arrival times of photo-electrons. There is a number of commercial laser that comply with the above criteria. After several tests between different kind of lasers the one chosen is the LDH-P-C-405M from Picoquant Fig. 5.6 with the following characteristics:

- Wavelength: 405 nm $\pm$ 10 nm.

- Pulse FWHM: <600 ps.

- Average Power (@400MHz): 20 mW.

- Energy/pulse: 500 pJ.

Below the guidelines for the light distribution chain are listed:

Figure 5.6: The LDH-P-C-405M laser head by Picoquant.

- High sensitivity monitors of the transmitted light at the end point of each individual section of the distribution chain must be used to ensure online control of the system stability and to have information for applying feedback corrections to the source parameters, if needed.

- The optical path must be minimized in order to limit the light loss due to self-absorption in the optical fibers. The number of cascade distribution points must also be minimized to reduce the unavoidable loss in the coupling between different sections.

- The laser source and its control electronics should be located outside the muon ring in order to avoid perturbation of the local fringe field induced by the current flow used to excite the laser.

- Optical fiber selection: for long distances fibers with high robustness against solarization or other aging effects due the large values of transmitted light intensity. For shorter distance these requirements are less severe so cheaper fibers could be used also for budget reason.
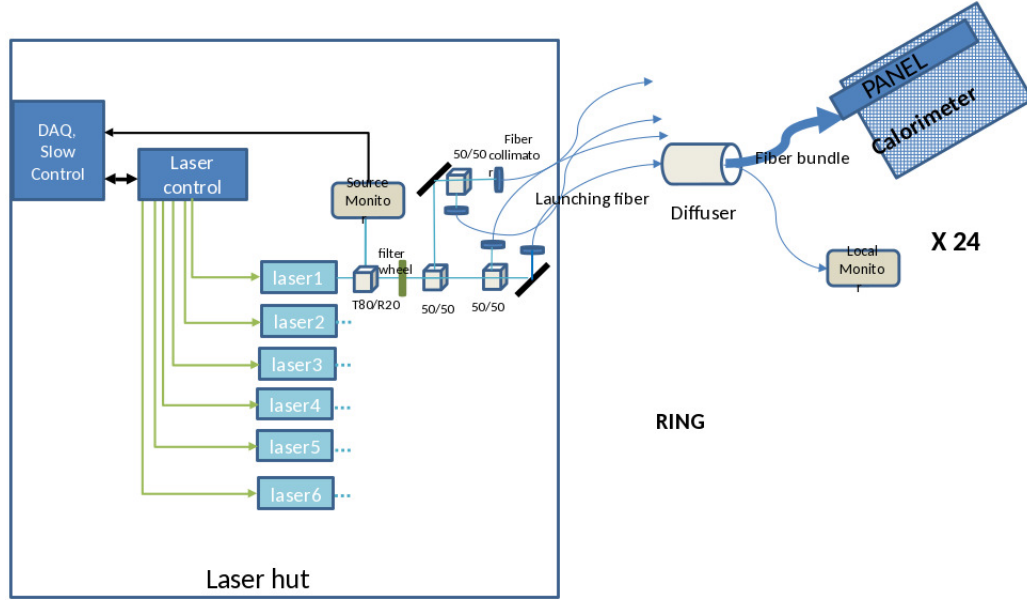
Figure 5.7: A schematic view of the laser calibration system.

The geometry adopted which fulfills all these requirements is shown in Fig.
5.7. The light generated by the LDH laser head is divided into 4 parts,
coupled into the launching fibers and sent to the secondary distribution
points located near each calorimeter station. The light source will be
composed by 6 synchronized laser. The choice of more than one laser was
due to the necessary intensity needed to illuminate all the crystals. With this
scheme synchronization is important. This will be ensured using a single laser
crate "Sepia" from Picoquant which has the capability to control up to 8 laser
synchronizing them up to some picoseconds with either internal or external
trigger Fig. 5.8. The laser source together with the optics and fiber couplers
will be located onto an optical table inside a laser hut, as shown in Fig. 5.9.
24 silica fibers (20 dB/Km attenuation at 400 nm), one per calorimeter, 25 m
long, route the light to secondary distribution point located close to the
calorimeter. A small fraction of the light exiting each laser source and each

Figure 5.8: Laser crate "Sepia". Each laser head LDH-P-C-405M will be coupled to its driver (the crate contains up to 8 drivers).
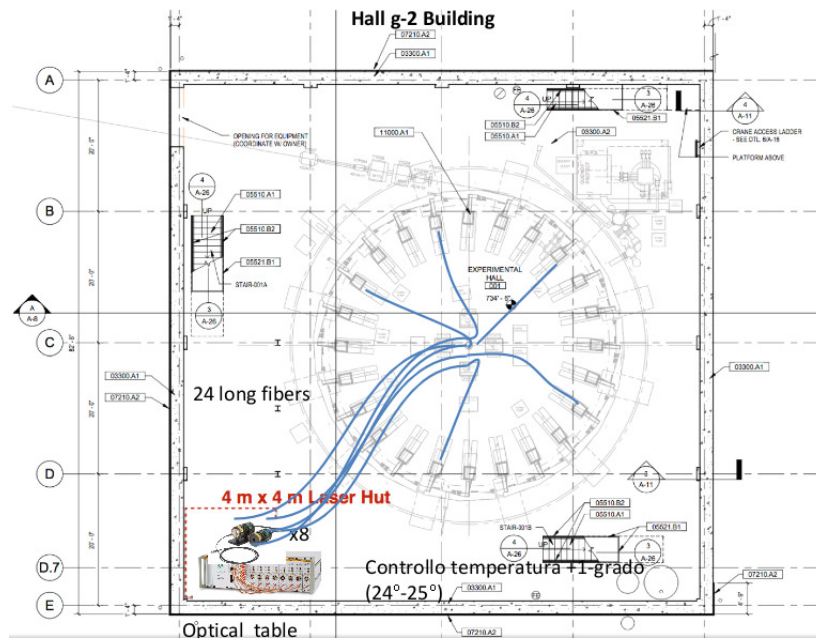

Figure 5.9: Scheme of the laser hut position inside the MC-1 building.

light distributors is detected by dedicated detectors used to monitor the intensity of the calibration light. Signals from these "monitors" are sent back to the DAQ system for both online checking of the system stability and further offline monitoring of the calibration signal. Several test were performed to find the best solution for the distributors that should be placed near the calorimeter. The requirements are uniformity and stability of the light output without a significant drop in intensity. Studies were performed comparing the performances of the integrating sphere and diffuser [65]. The intrinsic properties of the integrating sphere permit a very high level of uniformity of the light output as can be seen in Fig. 5.10 a). The drawback of the sphere is a very low value of the transmitted light, which is almost 10^{-4} times the intensity of the input per single fiber. Comparison with the diffuser, in Fig. 5.10, shows that the sphere has a better level of uniformity but the diffuser, shown in Fig. 5.11, with its good uniformity and a very high level of the output light intensity, was the solution adopted.

5.3   Front Panel & mechanics

The coupling of the laser calibration system with each calorimeter requires special care; all the fibers of the bundle must be locked properly to guarantee the correct light-path to the crystal. Moreover all the system should be in a light tight environment to avoid external light noise. A big issue is given by the dimensional constraints given. The maximum depth available is of only few cm. The small space available doesn't permit to face directly the fibers of the bundle to each crystals. For this reason a specific panel was designed for each calorimeter. The g-2 front panel shown in Fig. 5.12 is a delrin plate with 54 holes and grooves; the grooves permit to place the fibers in the right
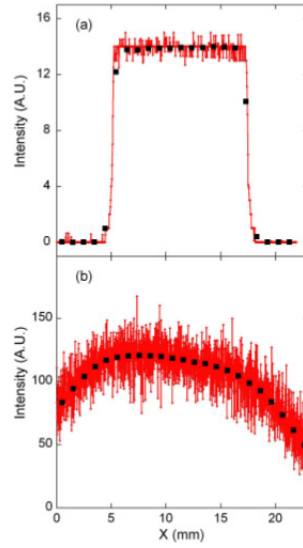
Figure 5.10: Experimental luminance profiles of a single pixel row (daggers) and average 900 pixels (squares), for sphere a) and diffuser b).
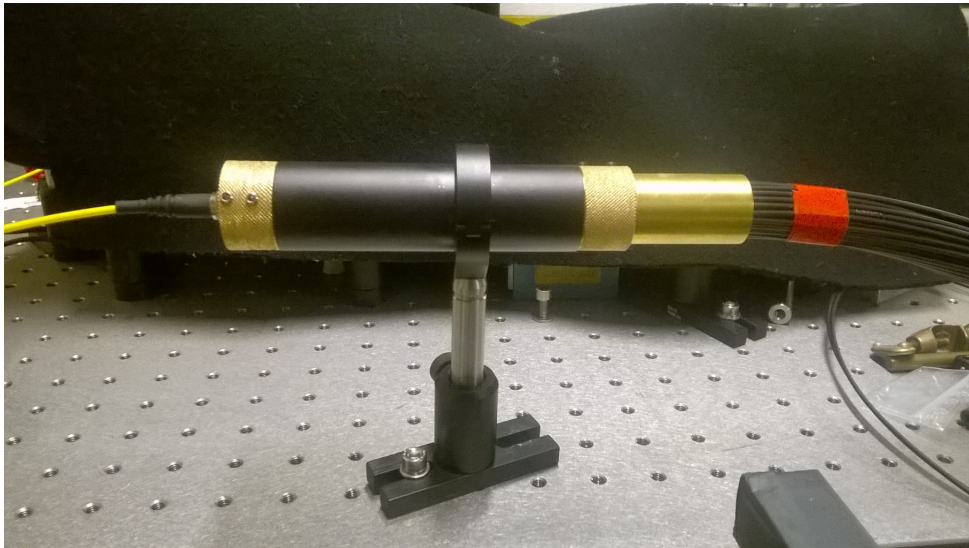

Figure 5.11: Picture of the diffuser used for the calibration system of the E989 experiment.

position ending to an hole where a 45° prism for each hole is placed, which permits to deflect of 90 degrees the light coming from the fibers without bending them. A PVC plate is placed in front of the g-2 front panel to ensure light tightness of the laser calibration box and subsequently to the calorimeter system to which the box is coupled with.

Figure 5.12: Picture of the g-2 front panel. Each hole in the delrin plate houses a 8x8 mm^2 45° prism which deflects the light coming from the fiber placed inside the groove.

In Figs. 5.13 and 5.14 the design of a light tight box for the laser calibration system is shown.

Fig. 5.13 shows how the laser calibration box, containing the diffuser, the fiber bundle and the front panel to route the fibers to the crystals, is positioned with respect to the calorimeter box. Laser comes from the right through the 25 m long silica fiber coupled to the diffuser placed inside the box, Fig. 5.14. From the diffuser a bundle of fibers drive the light to the crystals, as already explained. Production of the box and the delrin plate is in charge of the Laboratori Nazionali di Frascati (LNF) mechanical workshop.
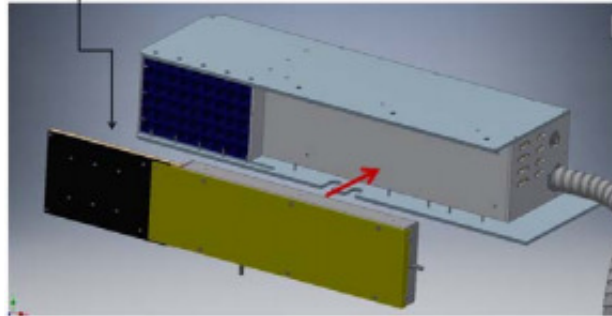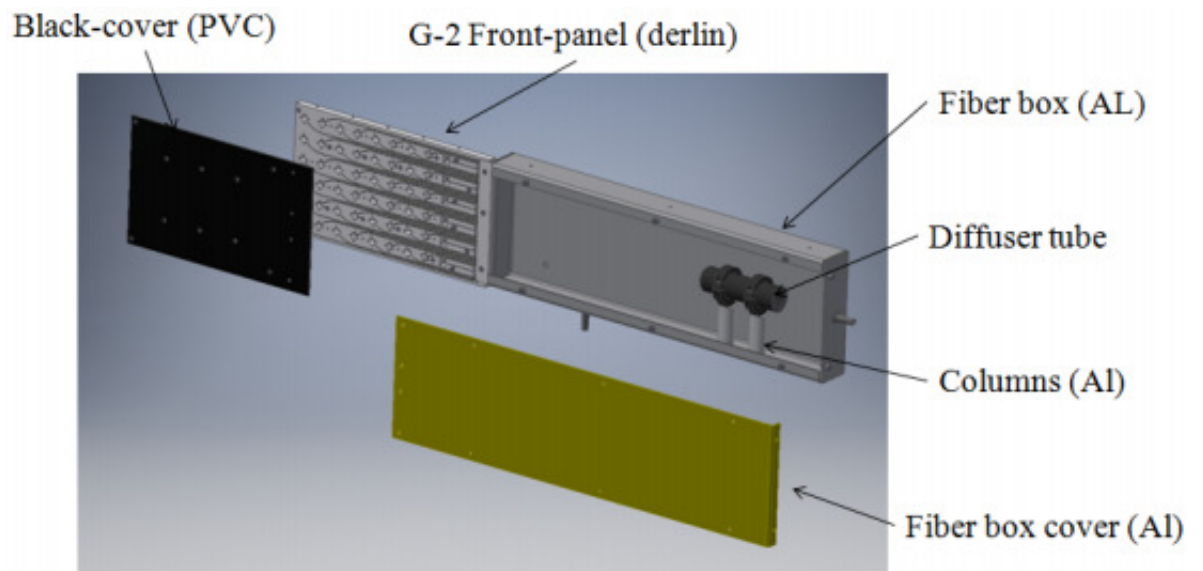
Figure 5.13: Laser calibration box and calorimeter box.

Figure 5.14: Details of the laser calibration box mechanics.

5.4   Monitors

5.4.1   Source Monitors

The source monitors (SM) are designed to monitor the instabilities of the laser system to later apply a correction in the analysis: assuming the laser-induced signals from all calorimeters elements (Sci) and the monitors (Sm) are subject to the same laser fluctuations, these kind of fluctuations should be eliminated in the ratio Sci/Sm. These ratios should then reveal fluctuations in the calorimeter response, provided other fluctuations in Sm are stable to degree required. The guidelines followed to optimize the design of the monitor are:

- zero gain PIN diodes are used which are much more stable than SiPMs to variations in bias voltage and temperature;

- the system is exposed to high light level ($\sim 30\%$ of the laser light) to minimize photostatistics fluctuations;

- dedicated electronics specifically designed to get high stability;

- use of a redundant system with three photodetectors for each monitor;

- minimize pointing fluctuations incorporating diffusion and mixing elements;

- use a radioactive source inside the monitor, for absolute calibration.

Fig. 5.15 shows a schematic illustration of a monitor geometry following the above criteria. a sketch of the geometry of the design of a source monitor which follows the above considerations.
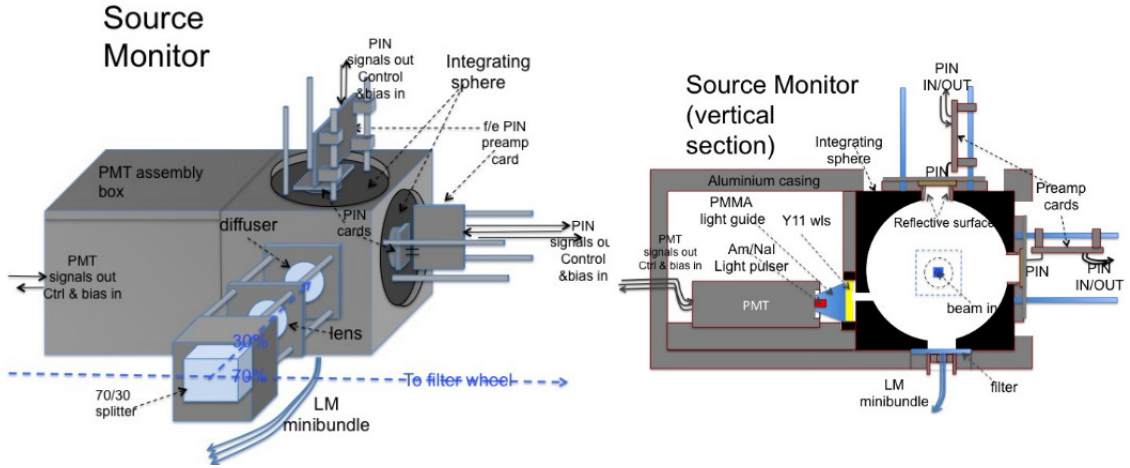
Figure 5.15: Schematic illustration of a monitor geometry.

A 70/30 beam splitter routes 30% of the laser light to the monitor. To minimize beam pointing fluctuations to the monitor photodetectors the light is injected to an integrating sphere. The task of this device is to mix the light with multiple reflections inside. With this procedure the light that comes out from the sphere ports has a high level of uniformity. Three different ports are used for the purpose of the source monitor. In two ports two large area Pin Diodes are placed for redundancy. The PIN diodes are relative slow (~ 10 ns pulse width) compared to laser pulses but fast enough to be integrated by their electronics for stability. rom the third port three fibers come out: one goes to the other monitor photodetector: a photomultiplier (PMT) equipped with an NaI in which a quantity of ^{241}Am is deposited. This radioactive source serves as absolute reference for the monitor system; the other 2 fibers go to another monitor system, called Local Monitor (LM), as reference signal.
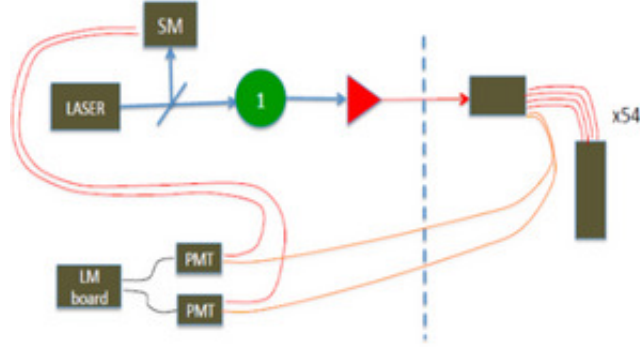
Figure 5.16: Scheme of the local monitor.

5.4.2 Local Monitors

The source monitor task is to correct for possible fluctuation of the laser source independently from the distribution chain. To correct for possible gain fluctuations induced by the passive elements of the distribution chain, due to aging effect or mechanical vibrations, a local monitor system is required to keep the systematic error under the required value of 0.02 ppm. For this reason this second monitor was designed. Following the same criteria of a redundant system with an absolute reference the purpose of this device is to control any kind of fluctuation due to the optical elements of the distribution chain, see Fig. 5.16.

This monitor is designed to serve each calorimeter. It detects the same light of the crystals in the calorimeter; this value is orders of magnitude lower than the light that reaches the source monitor and therefore it doesn't allow the use of PIN diodes. Several test were performed to chose an appropriate photodetector; the best solution is to use PMTs, because of their high level of gain and their intrinsic stability. The only drawback is the high current produced which forbids placing the local monitor close to the calorimeter

because it perturbs the fringe field when shielded. The solution adopted is to place the two PMTs for each calorimeter in the laser hut; each PMT receives two signals: one coming from the distribution chain through a long fiber and a second coming from the source monitor which serve as a reference signal. Relating the signal coming from the distribution chain to the reference signal it is possible to correct for the gain fluctuation due to the distribution chain elements. Care must be taken to stabilize the fibers coming from the calorimeters to the PMTs against temperature or mechanical and optical variations.

5.5 Electronics

Specific electronics system must be designed to accomplish all the task of the calibration system and in particular refers to:

- Laser control board;

- monitoring board.

5.5.1 Laser Control Board

The laser control board is specially designed to control and manage the light source. A picture is shown in Fig. 5.17. The clever part is a beagle-board processor with a Linux operating system. Through TTL signals it gives trigger to the Sepia driver; this permits to send different patterns of light pulses to the calorimeters and operate in different modes:

- standard calibration;

- fixed pattern;

- flight simulator mode.

The standard calibration mode consist in sending laser pulses during the data taking inside the muon fills with a rate of 10 kHz. Each fill has a length of 700 μs and consequently 7 laser pulse per fill. In the next fill the laser pulses are shifted by 5 μs. To have a complete scan a fill 140 muon fills are needed but to reach a good statistics about 2000 fills are necessary. This is the main operation mode for the calibration of the g-2 experiment.
The fixed pattern mode gives the possibility to send continuous laser pulses at a fixed rate for debug and testing. An interesting operation mode is the flight simulator mode. In this mode the laser driver board set up an exponential pulse pattern simulating a muon fill with a variable rate in a window of 700 μs. This gives the opportunity to have specific laser run with the muon beam characteristics during test or commissioning period.

5.5.2   Monitoring board

The monitoring board (MB) is designed to process the calibration signal of the Source Monitor and the Local Monitor. It's a smart device which acquires signals from the monitor (calibration signal), the accelerator (Begin of Fill BOF, and End of Fill EOF) and environments (Temperature) and send them to the wave-form digitizers (WFD) and to a local digitization. It also acts as Voltage supply for the monitors. The smart part of the board is an FPGA which executes control procedure and acts in case corrections to HV or other settings are needed. In Fig. 5.18 a picture of the first prototype is shown. The MB has a local DAQ as shown in Fig. 5.19. The information acquired by the MB will be sent also to the Slow control system. The controller of the local DAQ manage the data flow from the MB to the Slow Control and in
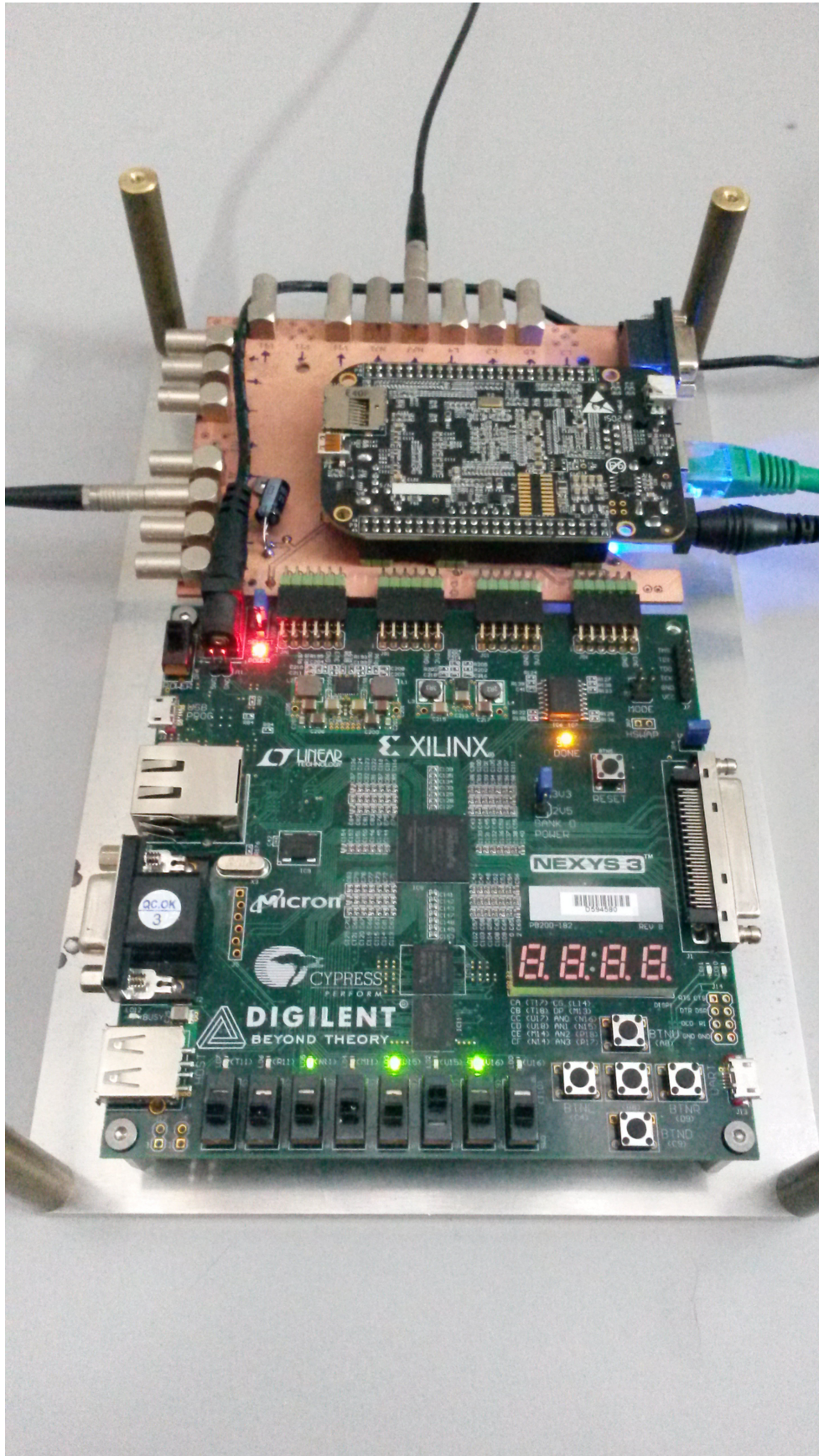
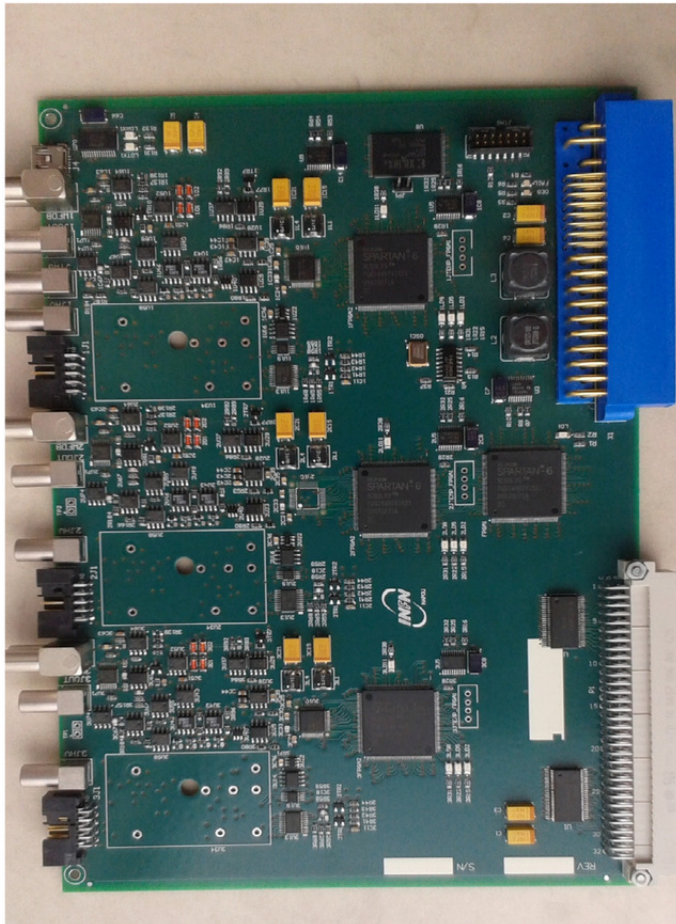Figure 5.17: Picture of the Laser Control Board.

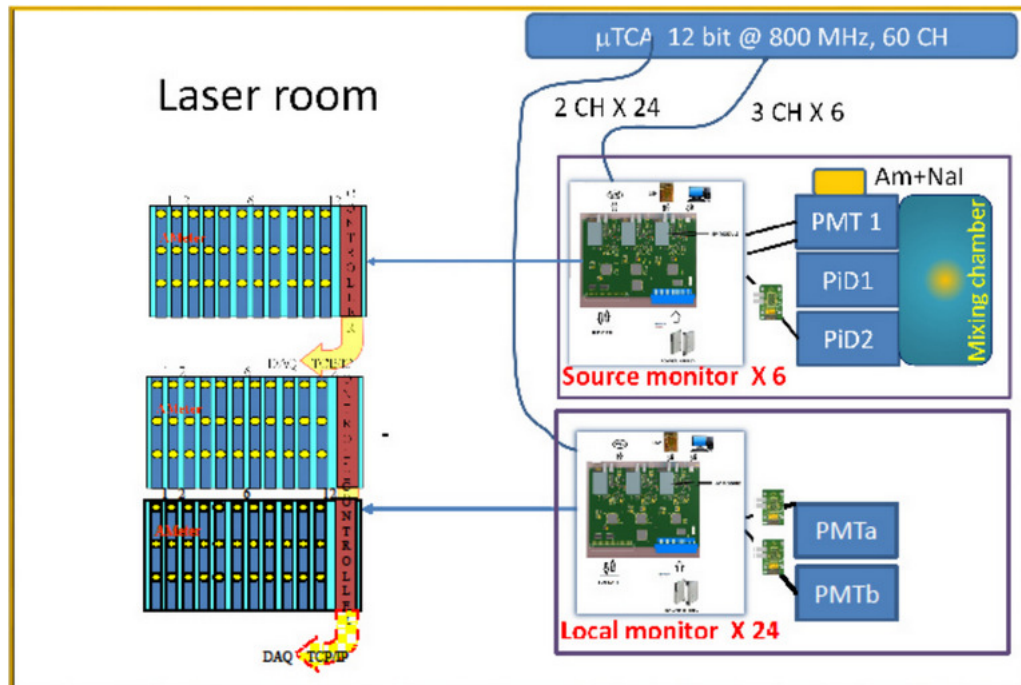Figure 5.18: First prototype of the Monitoring Board designed by INFN Naples.

Figure 5.19: Calibration DAQ scheme.

particular

- Temperature;

- bias voltage;

- electronic gain.

Chapter 6

Test Beam of the Laser Calibration System

Several test beams were performed during these years to test calorimeter prototypes with a more refined design time after time. The test beam presented in this work, with its laser calibration data, was performed from 29th February to 7th March at the Beam Test Facility (BTF) [67] of Laboratori Nazionali di Frascati (LNF). This test was planned and organized by the Laser Calibration group as a final test of the laser calibration system. It was the occasion to test all the different components of the system developed in different laboratories in Italy, coupled together, to test the effective operation of the full laser calibration system on a small calorimeter prototype.

In Fig. 6.1 a sketch of the BTF setup is shown used that will be described in the following. The specific goals for this test beam were:

- Test of the full line calibration system(from the laser control board to the photodetectors).
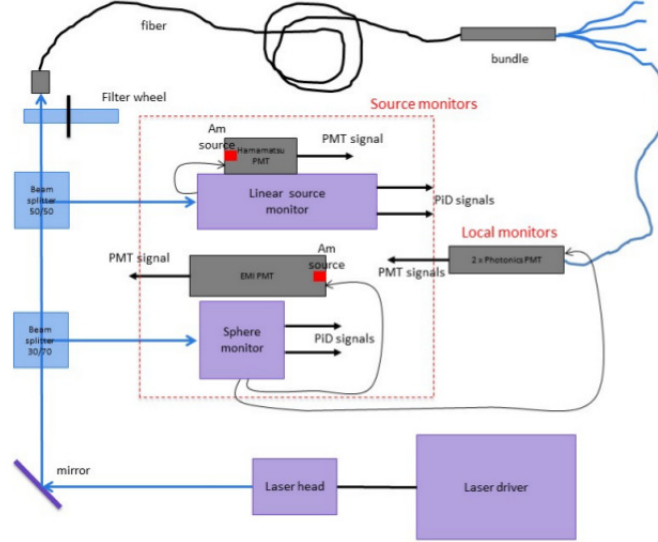
Figure 6.1: Sketch of the BTF setup.

- To compare the laser signal the e$^-$ beam to obtain the equivalent luminous energy of the laser.

- Test of the SiPM and Bias Voltage.

The Frascati BTF provides a highly collimated electron beam with a 50 Hz repetition rate and a maximum energy of 500 MeV. The BTF can run in electron or positron mode depending on the user choice. Its duty cycle is dependent on the DAΦNE collider [70] working condition. For this test beam it was chosen to work at low beam intensity with an average of one electron per pulse. The electron beam has a transverse dimension of about 250μm and a mean position stable in time.
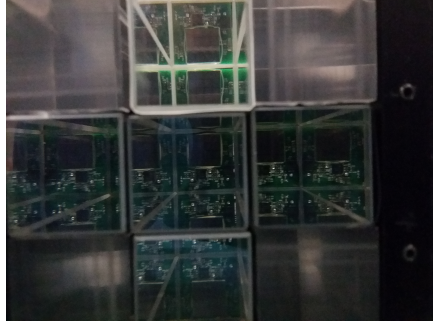
Figure 6.2: A front view of the calorimeter. Different crystal wrappings can be observed (top crystal in white wrapping). It is possible to recognize the real crystal from the fake Plexiglas ones, looking at the SiPM image reflected on the rear side.

6.1 Setup

6.1.1 Calorimeter

The calorimeter was positioned on a movable bench in order to match the position of the electron beam. It consist of a small scale prototype of the calorimeter that will be used for the E989 experiment described in chapter 4; it was composed of only five elements[1] arranged in a cross-like configuration with four additional mock Plexiglas crystals to create a 3×3 array. The sensitive elements used are $2.5 \times 2.5 \times 14$ cm^3 high-quality PbF$_2$ crystals [68]. Four of them were wrapped in black absorbing Tedlar, while the remaining one was wrapped in reflective white Millipore paper, Fig. 6.2.

A 16-channel Hamamatsu SiPM was glued to the rear face of each crystal. The five SiPMs detect both the Cerenkov light generated by the electron beam and the calibration photon pulses. Laser calibration pulses were guided to the front face of each calorimeter element by means of optical fibers, each ending on a reflective right angle prism so as to inject the light in a direction

---

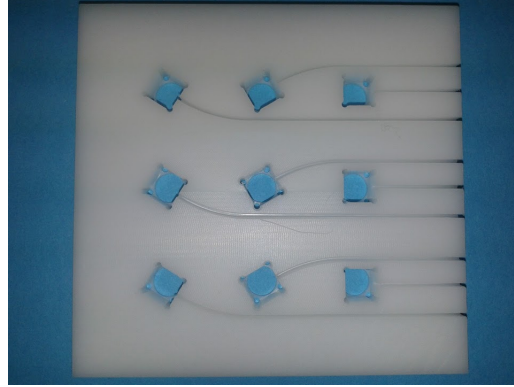[1]Considering crystal and its associated photodetector a single element.

Figure 6.3: Picture of the front panel prototype used. This is a small scale prototype of the front panel that will be used for the full calorimeter in the experiment. Each hole houses a 45° prism and the grooves drive the fiber to the prisms.

parallel to the crystal axis. The prisms and the terminal of the fibers are held by a Delrin panel manufactured by the Laboratori Nazionali di Frascati mechanic workshop, Fig. 6.3, that is positioned in front of the calorimeter. Each SiPM has two connectors: a PIN connector and an HDMI one. A custom PIN-to-MCX cable is used to connect the SiPM to the digitizer; the HDMI cable provides the bias Voltage through a custom breakout board developed at the University of Washington. This breakout board has 16 channel for each different SiPM. The bias voltage could be provided in two different ways: a single voltage to all the 16 channels or two different biases via two different lines of 8 channels each. The breakout board is also linked to a beagleboard microprocessor [71] which is used to run control procedures and set parameters of the SiPM frontend electronics, e.g. set gain values, read temperatures. SiPM are very sensitive to temperatures, and it is important to have a continuous monitoring of this parameter together with a cooling system. For this test beam it was sufficient to maintain an acceptable temperature, stable in time, with a simple system composed by a fan unit.

6.1.2 Laser source

The laser source is a LDH-P-C-405M pulsed laser by PicoQuant, as described in the previous chapter, with a maximum energy of 1 nJ per pulse, a pulse width of about 700 ps, with a wavelength of 405 ± 10 nm. The repetition rate can be varied from from 2.5 MHz to 40 MHz using the PDL 800-B laser driver by PicoQuant. A custom electronic board permits to select also specific values of the repetition rate down to few Hz.

6.1.3 Laser distribution system

In the real experiment the laser system must feed almost 1300 channel plus all the monitoring system for a total of ~ 1350 channels. For this reason an appropriate light distribution system was developed and should be tested. In this test beam part of the laser light is driven by beam splitter cubes to the monitoring system. The laser beam is then coupled and focused into a 400 μm diameter and 25 m long fused silica fiber, with an attenuation of 20 dB/km at 400 nm. This fiber was used to simulate the running condition of the E989 experiment. The light output of the fibers is collimated and transmitted through an engineered diffuser produced by RPC Photonics, consisting of a structured microlens arrays, which transform a gaussian input beam into a flat top one [65]. The light from the diffuser is then driven to the calorimeter through a fiber bundle made of 1 mm diameter and 3 m long PMMA. Five fibers of this bundle are connected to the light distribution panel faced to the 45° prisms; two other fibers are coupled to the two PMTs of the local monitor. To complete the system a motorized filter wheel is placed before the silica fiber to change the light intensity of the laser pulse reaching the calorimeter.
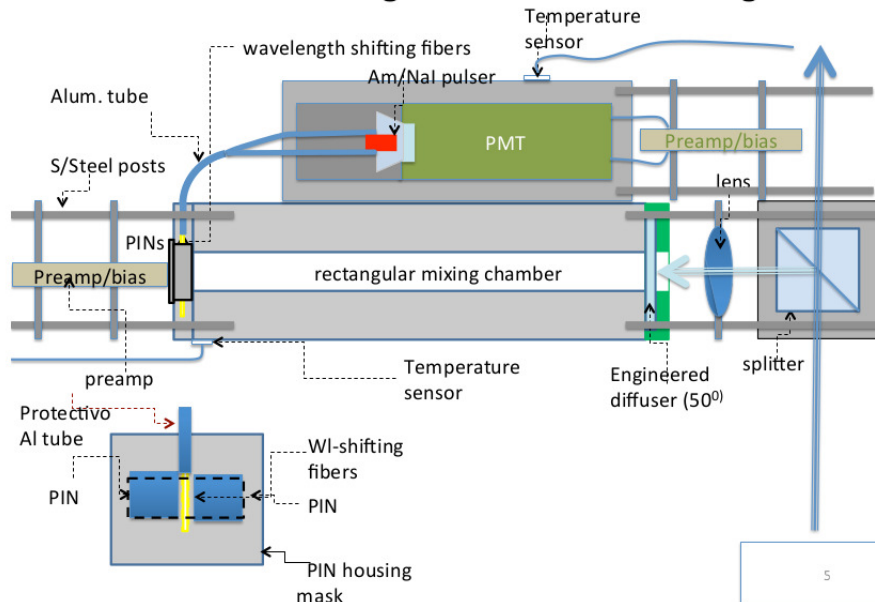
Figure 6.4: Schematic illustration of the alternative design of the source monitor used during the test beam.

6.1.4 Monitors

Monitoring systems are of fundamental importance to control all possible sources of fluctuations, for this reason it is important to study their result in this test beam. A local monitor (LM) system and two different design of the source monitor system (SM) were available for this test. The alternative design of the monitor consist in a different mixing element: a mixing chamber is used instead of the integrating sphere as shown in Fig. 6.4 Despite the differences from the hardware point of view the working idea is the same as well as the kind of signal produced, that can be seen in Fig. 6.5. As for the LM the design used in the test beam has been already described in chapter 5; two PMTs by Photonics model XP2982 will be used, which receive a fiber coming from the bundle that feeds the calorimeter and a reference signal coming from a source monitor. Each PMT sees two signals distant
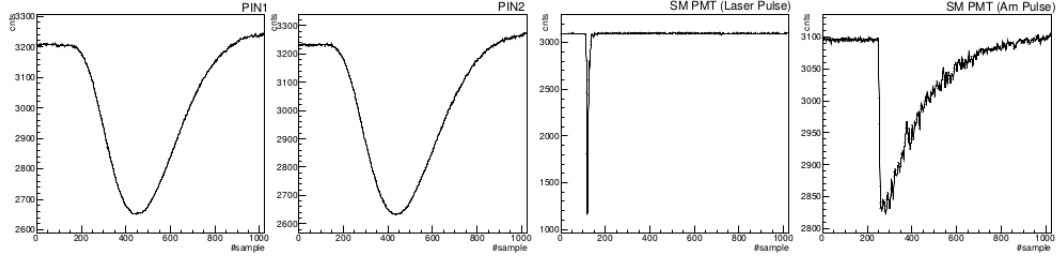
Figure 6.5: Signal produced by the source monitors. Starting from left: Laser signal in output from the pin diodes, laser pulse signal in output from the PMT, and americium pulse signal in output from the PMT.

~100 ns due longer path covered by the signal coming from the bundle as shown in Fig. 6.6.

6.1.5 DAQ

For this test 18 digitizers channel were necessary to process all the signals from the different devices. For that a CAEN DT5742, 16 channel 5 GS/s, and a CAEN DT5730B, 8 channel 500 MS/s, were used. Four separate triggers could initiate digitization and readout by the DAQ: a beam trigger, a laser trigger and an Americium trigger from each of the two SM being tested. Fig. 6.7 describes the trigger scheme and its configuration. In the data stream also temperatures from SiPM and environment were acquired.

6.2 Results

6.2.1 Calibration procedure

The procedure used during all the test beam was to have a calibration run after every change in the setup configuration and before every electron run.
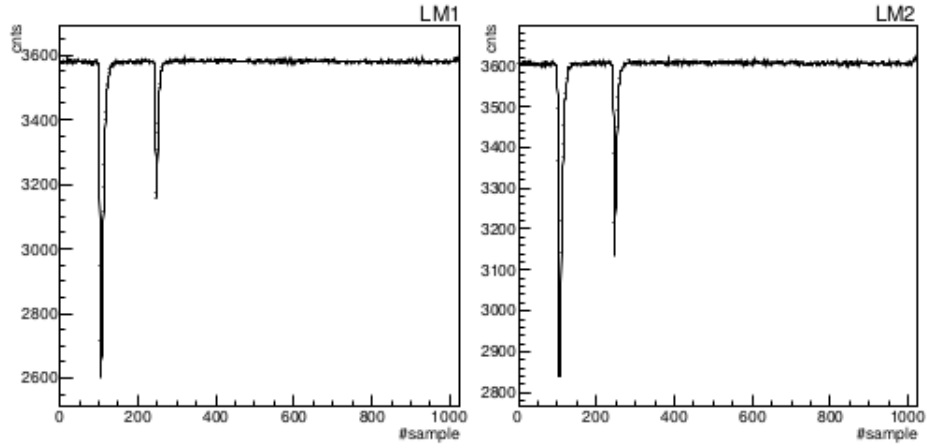
Figure 6.6: Signal seen by the PMTs of the local monitor. The first peak is the reference signal coming from the source monitors which arrives first and is also higher while the second is the signal at the end of the distribution system.
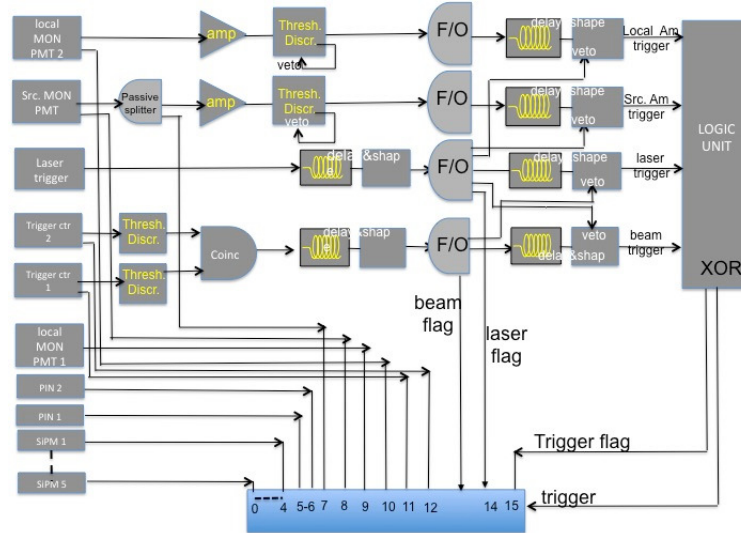

Figure 6.7: A scheme of the trigger used for the test beam.

This procedure tests all the functionality of the laser calibration system and also is useful to measure the equivalence between the ADC counts of the SiPM and the number of fired pixels. The calibration runs consist in a series of consecutive run with 6 different settings of the filter wheel; about 10000 events per runs were taken at a frequency of 50 Hz taking only some minutes per run. For each setting it was measured the mean μ and the standard deviation σ of the distribution of each of the five SiPM used. The signal L observed by each SiPM is given by $L = k\nu$ where k is the proportionality constant and ν is the number of fired pixels. The width of the signal L is given mainly by three main contributions: 1) the electronic noise σ_N, 2) the Poisson statistics of the pixel fired $\sigma_P = k\sqrt{\nu}$, 3) the intrinsic laser pulse fluctuations $\sigma_L = \alpha k\nu$, where α is the average relative laser intensity variation, which has been measured to be less than 1%. There are other factors that contributes to L proportionally that arise from the statistical variation in the number of photons incident on the SiPM photocatodes and from fluctuations in the amplification mechanism. Based on this model and assuming statistical independence of the sources of fluctuation, the dependence of σ^2 as a function of the measured light intensity can be obtained

$$\sigma^2 = \sigma_N^2 + kL + \beta L^2 \tag{6.1}$$

where the factor β includes all the contributions proportional to L. In Fig. 6.8 is shown a typical fit of the variance versus signal strength [69].
The values measured are between 600 and 800 fired pixels, depending on SiPM, bias voltage and SiPM temperatures, in open position of the filter wheel. Considering the total number of pixels of a single SiPM of ~ 57600 these values are about 1% of the total [68], applying a correction about
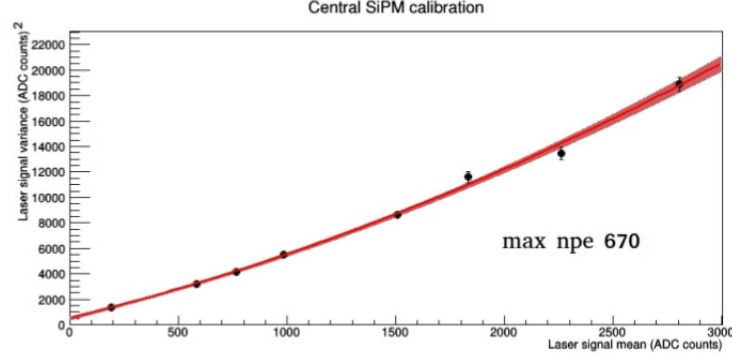
Figure 6.8: Calibration signal of a SiPM width with fitted curve.

saturation expected to be of the order of 0.5%, which has a negligible impact for these calibration results. In the electron runs the laser was also pulsed at the same rate of the electron beam, at 50 Hz. This was done in order to exercise both Source and Local monitors, providing a reference to stabilize the SiPM response over the time needed to complete the data taking. The calorimeter response is calculated as the sum of all the SiPMs normalized to response of the central one after correcting for the laser calibrations. This is guided by the fact that the beam is strongly focused on the central crystal, which receives $\geq 90\%$ of the beam energy and because the light transmitted to the dummy diagonal mock crystals is expected to be very small. In Fig. 6.9 the calorimeter response with the single and multiple electron spill is visible; the fit is performed with a sum of Gaussian distributions for the different electron peaks where the means are assumed to be linearly related to the number of electrons and the widths with their square root. The assumption on the widths is based on Poisson statistics of the number of fired pixels and on a contribution from the beam energy spread. The fit is typically well behaved and returns the mean value of the single electron peak in ADC counts. Dividing this value by the value obtained by the calibrations
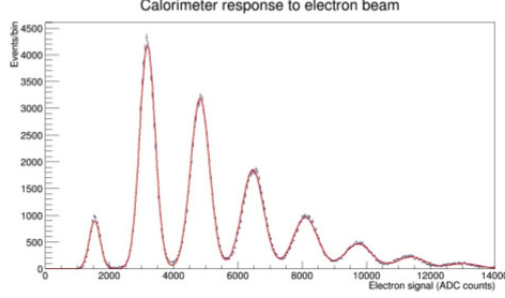
Figure 6.9: Calorimeter response showing single and multiple electron peaks, together with fitted curve.

and by the beam energy the results is the average number of pe/MeV; the result is 0.9 pe/MeV for the black wrapping which is consistent with the result presented in [68].

Using the open position of the filter wheel is possible to obtain the equivalent luminous energy of the laser, providing to relate this value to the beam energy of 450 MeV and the single electron mean. During this test beam values obtained are around 800 MeV, which corresponds to a measured light power before the filter wheel of 11.2±1.1 pJ. This value can be scaled to the laser power predicted in the final full calorimeter system, expected to be 141 pJ before the filter wheel. With this value the equivalent maximum energy seen by the calorimeter would be 800 MeV $\times$ 141/11.2 pJ $\sim$ 10 GeV [2].

6.3   Stability of the system

One of the task of this test beam is to measure the stability of the monitoring system developed for the experiment. In fact the energy of the electron incident on the calorimeter recorded by the SiPMs is expected to be

---

[2]Assuming an initial laser power of 1nJ.

affected by source of fluctuations; mainly temperature variations and also small bias voltage variations. Only by monitoring this variations through the response of the SiPMs to the laser pulses during data taking is possible to track this kind of variations and correct for it, given the right accuracy of the monitoring system. In mathematical terms the response of a SiPM to the electron beam during time is given by

$$r_{el}^{SiPM}(t) = R_{el}^{SiPM} \times f_{gain}^{SiPM}(t), \tag{6.2}$$

where R_{el}^{SiPM} is the real real signal and $f_{gain}^{SiPM}(t)$ are the time-dependent sources of gain variations related to the SiPM, while the response to the laser pulses is given by

$$r_{laser}^{SiPM}(t) = R_{laser}^{SiPM}(t) \times f_{gain}^{SiPM}(t) = R_{laser}^{SiPM'} \times f_{laser}(t) \times f_{chain}(t) \times f_{gain}^{SiPM}(t), \tag{6.3}$$

where the f terms are gain fluctuations terms due to the laser and the distribution chain and are monitored by the SM and LM respectively. Therefore the corrected electron beam signal for a given time is:

$$R_{el}^{SiPM} = \frac{r_{el}^{SiPM}(t)}{f_{gain}^{SiPM}(t)} = \frac{r_{el}^{SiPM}(t)}{\frac{r_{laser}^{SiPM}(t)}{R_{laser}^{SiPM'}}C_{SM}(t)C_{LM}(t)}, \tag{6.4}$$

where C_{SM} and C_{LM} are the corrections given by the SM and LM respectively. The result of the correction procedure is shown in Fig. 6.10 where the variations, relative to the first point, in the raw electron data after four continuously running hours are shown before and after correction (see figure description for details) [67]. The corrected electron data correspond to the raw electron data divided by the corresponding laser data after correction for laser intensity and light distribution stability. Each data points represent data averaged over approximately 20 minutes of running.
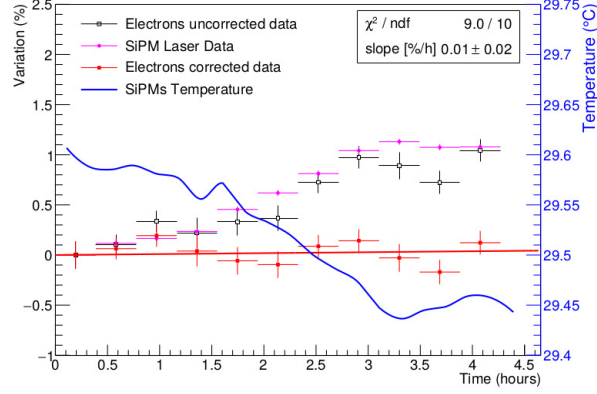
Figure 6.10: Variations in the measured energy of the electron beam and of the laser signals during four hours of data acquisition. The black (magenta) open circles show the gain fluctuations in the raw electron (laser) data while the full-red circles are the corrected data. All the variations are evaluated with respect of the first data points. SiPM temperatures recorded during the same period are also shown as blue line.

As shown in Fig. 6.10, electron data without any corrections, in black circles, exhibit a positive drift of about 1.2%/4h and laser data, magenta circles, track electron data. However to apply the laser correction, the laser data should be corrected before for laser intensity and transmission efficiency of the laser pulses from source to calorimeter. All these variations taken into account for corrections are shown inf Fig. 6.11 [67]. The SM correct for the stability of the laser intensity. The PiDs measured a variation of 0.2%, as shown in Fig. 6.12 and by the black solid circles in Fig. 6.11. Verification of this result is obtained comparing the signal of the SM PMT (open diamonds) which views the same laser pulse together with the [241]Am absolute reference, which provides all the correction to the PMT response which do not depend directly on laser fluctuations. Unfortunately the activity of the americium
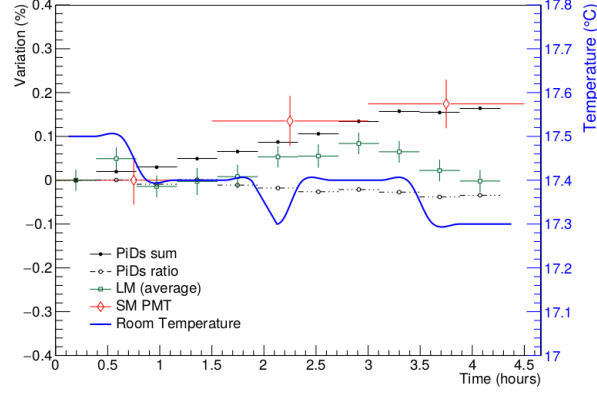
Figure 6.11: Stability of the laser calibration system. Solid black circles show the variations in the laser intensity as measured by the Source Monitor whereas the open squares represent the fluctuations in the laser light after distribution as recorded by the Local Monitor. Open diamonds represent SM PMT signals. As in Fig. 6.10 are referred to the first data point. The ratio between the two PiDs of the SM is also shown (black open circles). Room temperature in the same period is shown by the blue line.

radioactive source incorporated in the pulser used for this test beam was very low, requiring longer period of data taking, which were not available during this test, to have a more accurate comparison. Nevertheless, data presented confirm the same trend measured by the PiDs with their statistical accuracy. The variations in the laser intensity, represented by the black points in Fig. 6.11, correspond to variations in the average of the two PiDs viewing the same laser pulse in the SM. These data monitor laser stability with an accuracy of 0.003% per point (23 minutes of data taking, corresponding to $\sim$ 26000 events). Given the large number of photoelectrons generated in each PiD (almost 10^6/pulse) the expected statistical uncertainty per pulse is $<$ 0.1% or 0.0006% for the 26000 pulses collected. The much larger statistical error observed indicates that it is most likely driven by the noise introduced
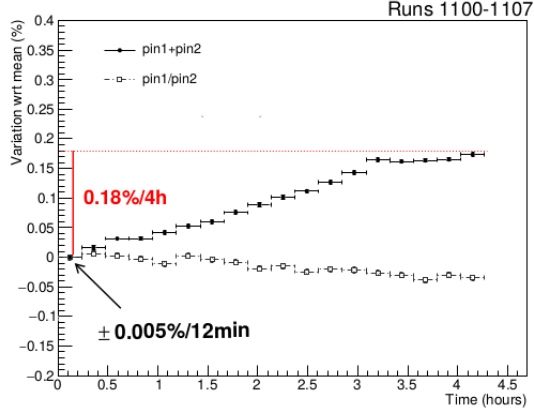
Figure 6.12: Pin stability data over 4 hours of data. As can be seen the overall drift is ~0.2%. The total Pins precision is then 0.005%/12 min.

by the prototype of the shaping amplifier used. This result will improve using the final version of the dedicated electronic that will be used in the experiment. Fluctuations related to the light distribution chain are measured by the LM system. They correspond to the fluctuations in the ratio of the signal from the end of the optical transmission to the signal of the source, monitored by the SM. Since both of the signals are detected by the same PMT, and separated about 100 ns, this ratio should be insensitive to fluctuations in the PMT gain. The redundant system ensures a better accuracy for this. In Fig. 6.13 data of the SM PMT and LM ratio can be seen, which show a statistical accuracy of 0.02%/12 min while in Fig. 6.11 data of the mean of the fluctuations are shown as open green squares.

To conclude an important information is to compare variations of the SiPMs with temperature variations measured by the sensors incorporated into the SiPM front-end electronics (blue line in Fig. 6.10). It is clear, from this comparison that mainly SiPM gain variations are related to temperature variations. Equivalent dedicated temperature measurements close to PiDs
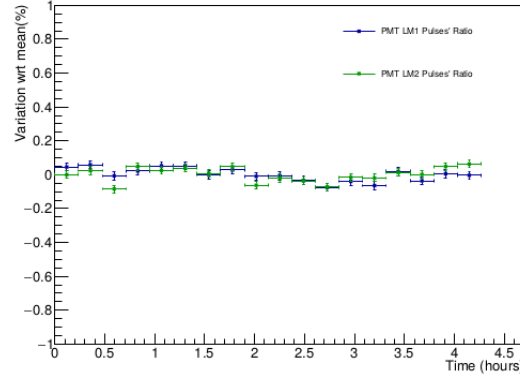
Figure 6.13: Data showing LM stability over 4 hours of data. The statistical accuracy obtained is 0.02%/12 min.

and monitor PMTs are not available in this test beam but, given the very low-power dissipation of the mentioned devices and their front-end electronics, the temperature of the experimental hall is a good approximation (solid blue line in Fig. 6.11). Temperature related variations of the LM PMTs are not relevant as previously explained. Since environment temperatures variations are small, one does not expect a large effect on the PiD on the basis of the expected temperature dependence (0.1%°C at 400 nm) [72].

Conclusion

The work presented in this thesis documents the development and the results obtained in the design, construction and testing of the Laser Calibration System for the E989 experiment which aims at precisely measuring the anomalous magnetic moment of the muon. This has been developed in 4 years, from the beginning of 2012 to 2016. Several laboratory test were performed, in order to find the best solution for a system which should be the first of its generation, with a total accuracy requested by the experiment of one order of magnitude better than the existing laser calibration system. The main goal of the system is to monitor the gain fluctuations of the SiPM at 0.04% statistical error and at 0.01% systematic one in the $700\mu s$ time window. This request together with the necessity to fit with all the other aspect and component of the experiment, accomplishes to make this a very hard task.

A Test beam at the Beam Test Facility of Laboratori Nazionali di Frascati (LNF) was organized as a final test of the R&D of the system. During this test it was verified that the calibration system is presently able to monitor and correct for laser intensity variations to 0.01% in two hours, and it has been proven that 6 lasers will be enough to illuminate all 24 calorimeters with an equivalent energy of as maximum 10 GeV per laser pulse. Test of the monitors system give satisfactory results: no significative difference were

found between the two designs of the source monitor both capable to correct for laser fluctuations despite the low level of the americium radioactive source activity and improvement can be obtained with the final version of the dedicated electronics for the pin diodes; local monitors were proven to be able to correct variations in the distribution chain on longer time scales obtaining correction factors that could be applied during data taking. Possible temperature related fluctuations of the monitors are not relevant because only the ratios of simultaneous events are necessary for the correction constants. All these results proved that the calibration system satisfies the requests and were submitted for publication in [67].

Data taking is expected to start in the middle 2017 and possible upgrades are already under development to be implemented in the future.

Acknowledgments

The successful implementation of an experiment demanding as the a_μ measurement required strong effort from a lot of people to coordinate the work in the construction. At the time of the redaction of this Thesis, the collaboration included:

- Argonne National Laboratory: J. Grange, R. Hong, J. Repond, P. Winter.

- Boston University: R. M. Carey, E. Hazen, N. Kinnard, J. P. Miller, J. Mott, A. Palladino, B. L. Roberts.

- Brookhaven National Laboratory: J. Crnkovic, W. H. Morse, H. Kamal Sayed, V. Tishchenko, K. A. Woodle.

- Budker Institute of Nuclear Physics: V. P. Druzin, I. A. Koop, I. Logashenko, Y. M. Shatunov, E. Solodov.

- Cornell University: W. F. Bergan, R. Bjorkquist, A. Chapelain, N. Eggert, A. Frankenthal, L. K. Gibbons, S. Kim, A. Mikhailichenko, Y. Orlov, N. Rider, D. Rubin, D. Sweigart.

- Fermi National Accelerator Laboratory: D. Allspach, K. Badgley, E. Barzi, B. Casey, S. Chappa, M. E. Convery, B. Drendel, H. Freidsam,

C. Johnstone, J. Johnstone, B. Kiburg, I. Kourbanis, A. L. Lyon, K. W. Merritt, J. P. Morgan, H. Nguyen, J. F. Ostiguy, C. C. Polly, E. Ramberg, M. Rominsky, A. K. Soha, J. Stapleton, D. Still, T. Walton, L. Welty-Rieger, C. Yoshikawa.

- University of Groningen, KVI: K. Jungmann, C. J. G. Onderwater.

- University of Illinois at Urbana-Campaign: P. Debevec, S. Ganguly, A. Kuchibhotla, S. Leo, K. Pitts, C. Schlesler.

- Istituto Nazionale di Fisica Nucleare - Sezione di Napoli: S. Catalanotti, R. Di Stefano, M. Iacovacci, S. Marignetti, S. Mastroianni.

- James Madison University: K. Giovanetti.

- Joint Institute for Nuclear Research, Dubna: V. Baranov, V. Duginov, N. Khomutov, V. Krylov, N. Kuchinskiy, V. Volnykh.

- KAIST: M. Gaisser, S. Haciomeroglu, Y. Kim, S. Lee, M. Lee, Y. K. Semertzidis, E. Won.

- University of Kentucky: R. Fatemi, W. Gohn, T. Gorringe, F. Han, L. Kelton, B. Plaster.

- Istituto di Fisica Nucleare - Laboratori Nazionali di Frascati: A. Anastasi, D. Babusci, G. Corradi, S. Dabagov, C. Ferrari, A. Fioretti, C. Gabbanini, D. Hampai, N. Raha, E. Rossi, G. Venanzoni.

- University of Liverpool: T. Albahri, T. Bowcock, J. Carroll, S. Charity, T. Halewood-Leagas, A. Herrod, B. King, S. Maxfield, J. Price, A. Smith, T. Teubner, W. Turner, M. Whitley, A. Wolski, M. Wormald.

- Lancaster University: I. Bailey, M. Korostelev.

- University of College London: S. Al-Kilani, R. Chislett, M. Lancaster, G. Lukicov, E. Motuk, T. Stuttard, M. Warren.

- University of Massachussets: D. Flay, D. Kawall, Z. Meadows.

- Michigan State University: M. Berz, R. Hipple, K. Makino, D. Tarazona, E. Valetov.

- University of Michigan: T. Chupp, M. Farooq, A. Tewlsey-Booth.

- University of Missisipi: J. L. Holzbauer, B. Quinn, W. Wu.

- Universitá del Molise: A. Gioiosa, G. M. Piacentino.

- Northern Illinois University: S. Chattopadhyay, M. Eads, A. Epps, G. Luo, M. McEvoy, N. Pohlman, M. Shenk, A. Springer, M. J. Syphers, S. Szustkwoski.

- Northwestern University: A. de Gouvea, H. Schellman.

- University of Oxford: B. Abi, F. Azfar, S. Henry.

- INFN Sezione di Pisa: A. Basti, F. Bedeschi, A. Lusiani.

- Regis University: F. Gray.

- Shanghai Jiao Tong University: C. Fu, B. Li, L. Li, H. Yang.

- Technische Universitat Dresden: D. Stockinger.

- University of Texas: J. George, J. L. Ritchie.

- Universitá di Udine: D. Cauz, A. Driutti, G. Pauletta, L. Santi.

- University of Virginia: L. P. Alonzi, S. Baessler, E. Friez, J. Fry, S. Goadhouse, D. Pocanic.

- University of Washington: M. Fertls, A. T. Fienberg, N. Froemming, A. Garcia, D. W. Hertzog, P. Kammel, J. Kaspar, K. S. Shaw, R. Osofsky, M. Smith, E. Swanson.

- York College, CUNY: K. Lynch.

I want to thank all the members of the Laser Calibration Group for all the support given in these years and the lessons learned from them. In addition I am very grateful to D. W. Hertzog and J. Kaspar, to have considered me as one of their student during the time passed working together. I would also like to thank all the graduate students and post-doc of the collaboration met in these years and in particular to A. T. Fienberg for the useful discussion on every aspect of the experiment, analysis, hardware, and for the fundamental support given during the Test Beam. It would be harder without his contribution. I am deeply grateful to: Prof. Giorgio Giardina, at the University of Messina, for the possibility given to me; my supervisor in Messina Dr. Giuseppe Mandaglio for all the help given in these years academically and socially; finally to my supervisor Dr. Graziano Venanzoni, for all the time spent with me in these three years, for the lesson learned from him and for trusting me since the beginning.

Bibliography

[1] W. Gerlach and O. Stern, Zeitschrift für Physik **9**, 353 (1922).

[2] J. Chadwick, Nature **129**, 312 (1932).

[3] C. Anderson, Phys. Rev. **43**, 491 (1933).

[4] I. Estermann, O. Simpson and O. Stern, Phys. Rev. **52**, 535 (1937).

[5] P. Kusch and H. Foley, Phys. Rev. **74**, 250 (1948).

[6] D. Hanneke, S. Forgwell and G. Gabrielse, Phys. Rev. Lett. **100** 120801 (2008).

[7] B. C. Odon, D. Hanneke, B. D'Urso and G. Gabrielse, Phys. Rev. Lett. **97** 030801 (2006).

[8] D. Hanneke, S. F. Hoogerheide and G. Gabrielse, Phys. Rev. **A83** 052122 (2011).

[9] T. Aoyama, M. Hayakawa, T. Kinoshita and M. Nio, Phys. Rev. Lett.**109** 111807 (2012).

[10] T. Kinoshita and M. Nio, Phys. Rev. Lett **90**, 021803 (2003).

[11] M. Kecht, The anomalous magnetic moment of the muon: A theoretical introduction, 2003, [hep-ph/037239].

[12] R. VanDyck, P. Schiwinberg and H. Dehmelt, Phys. Rev. Lett. **59**, 26 (1987).

[13] T. Lee and C. Yang, Phys. Rev. **104**, 254 (1956).

[14] C. Wu *et al.*, Phys. Rev. **105**, 1414 (1957).

[15] R. Garwin, L. Lederman and M. Weinrich, Phys. Rev. **105**, 1415 (1957).

[16] D. Hutchinson *et al.*, Phys. Rev. Lett. **131**, 1315 (1963).

[17] W. Louisell *et al.*, Phys. Rev. **91**, 475 (1953).

[18] H. Eland, Phys. Lett. **21**, 720 (1966).

[19] D. Kawall, *Statistical and Systematic Errors in fitting ω_a*, Muon *g-2* Internal Note No. 322, 1998.

[20] F. Farley, *Proposed high precision (g-2) experiment*, CERN Intern. Rep. No. NP/4733, 1962.

[21] J. Aldins *et al.*, Phys. Rev. Lett. **23**, 441 (1969).

[22] V. Auslander *et al.*, Phys. Rev. **91**, 475 (1953).

[23] J. Augustin *et al.*, Phys. Lett. **28B**, 517 (1969).

[24] M. Gourdin and E. de Rafael, Nucl. Phys. **B10**, 667 (1969).

[25] K. Crowe *et al.*, Phys. Rev. D **5**, 2145 (1972).+

[26] T. Kinoshita, B. Nizic and Y. Okamoto, Phys. Rev. Lett. **52**, 717 (1984).

[27] Muon g-2 Collaboration (G. W. Bennet *et al.*), Phys. Rev. **D73**, 072003 (2006).

[28] T. Kinoshita and M. Nio, Phys. Rev. **D73**, 013003 (2006).

[29] P. J. Mohr, B. N. Taylor and D. B. Newell, CODATA Group, Rev. Mod. Phys **84**, 1527 (2012).

[30] R. Bouchendira *et al.*, Phys. Rev. Lett. **106**,080801 (2001).

[31] R. Jackiw and S. Winberg, Phys. Rev. **D5**, 2396 (1972).

[32] C. Gnendiger, D. Stöckinger and H. Stöckinger-Kim, Phys. Rev. **D88** 053005 (2013).

[33] F. Jegerlehner, arXiv:1511.04473.

[34] M. Davier *et al.*, EPJ **C71**, 1515 (2011).

[35] Hagiwara *et al.*, JPG **38**, 085003 (2011).

[36] A. Aloisio *et al.*, hep-ph/0312056.

[37] BESIII Collaboration, arXiv:1507.08188.

[38] B. Krause, Phys. Lett. **B39**, 392 (1997).

[39] M. Knecht and A. Nyffeler, Phys. Rev. **D65**, 073034 (2002).

[40] K. Melnikov and A. Vainshtein, Phys. Rev. **D70**, 113006 (2204).

[41] J. Prades, E. de Rafael and A. Vainshtein, Adv. Ser. Direct. High Energy Phys. Vol.**20** *Lepton Dipole Moments*, 303 (2010).

[42] E. Eichten, K. D. Lane and M. E. Peskin, Phys. Rev. Lett. **50**, 811 (1983).

[43] P. Mery, S. E. Moubarik, M. Perrotet and F. M. Renard, Z. Phys. **C46**, 229 (1990).

[44] S. J. Brodsky and S. D. Drell, Phys. Rev. **D22**, 2236 (1980).

[45] S. P. Martin, hep-ph/9709356.

[46] U. Chattopadhyay and P. Nath, hep-ph/0208012.

[47] P. Fayet, Phys. Re. **D75** 115017 (2007).

[48] D. Tucker-Smith and I. Yavin, Phys. Rev. **D83** 101702 (2011).

[49] A. Czarnecki and W. J. Marciano, Phys. Rev. **D64**, 013014 (2001).

[50] Muon g-2 Collaboration, arXiv:1501.06858, (2015).

[51] T. P. Gorringe, D. W. Hertzog, *Precision Muon Physics*, arxiv:1506.01465v1 (2015).

[52] O. Rifiki, *The muon anomalous magnetic moment: a probe for the Standard Model and beyond*, Report approved for the H.L.Dodge Department of Physics and Astronomy (2014).

[53] A. Anastasi *et al.*, Nucl. Instrum. Meth **A824**, 716-717 (2015).

[54] D. Hertzog, *Next Generation Muon g-2 Experiment*, arxiv:1512.00928v1 (2015).

[55] R. Carey *et al.*, FERMILAB PROPOSAL-0989 (2009).

[56] L. H. Thomas, Nature **117**, (1926).

[57] V. Bargmann, L. Michel, V. L. Telegdi, Phys. Rev. Lett. **2**, 435 (1959).

[58] G. W. Bennet *et al.*, Phys. Rev. **D80**, 052008 (2009).

[59] E. J. Konopinski, Ann. Rev. Nucl. Sci. **9**, 99 (1959).

[60] X. Fei, V. Hughes and R. Prigl, Nucl. Inst. Meth. Phys. Res. **A394**, 349 (1997).

[61] A. Abragam, in *Principles of Nuclear Magnetism*, p. 173-178, Oxford U. Press, (1961).

[62] P. J. Mohr and B. H. Taylor, Rev. Mod. Phys. **77**, 1 (2005).

[63] W. D. Phillips *et al.*, Metrologia **13**, 179 (1979).

[64] J. L. Flowers, B. W. Petley and M. G. Richards, Metrologia **30**, 75 (1993).

[65] A.Anastasi *et al.*, Nucl. Instrum. Meth. **A788**, 43-48 (2015).

[66] V. Tischenko *et al.*, Phys. Rev. **D87**, 052003 (2012).

[67] A. Ghigo *et al.*, Nucl. Intrum. Meth. **A515**, 524 (2003).

[68] A. T. Fienberg *et al.*, Nucl. Instrum. Meth. **A783**, 12-21 (2015).

[69] A. Anastasi *et al.*, *submitted to Nucl. Instrum. Meth A.*

[70] M. E. Biagini *et al.*, **Brussels 1995, High energy Physics**, 377-379 (1995).

[71] Beagle board microprocessor: *http://beagleboard.org/BeagleBoard-xM*.

[72] Hamamatsu Si PIN Photodiode Datasheet, *http://www.hamamatsu.com/resources/pdf/ssd/s3590-08-kpin1052e.pdf*.